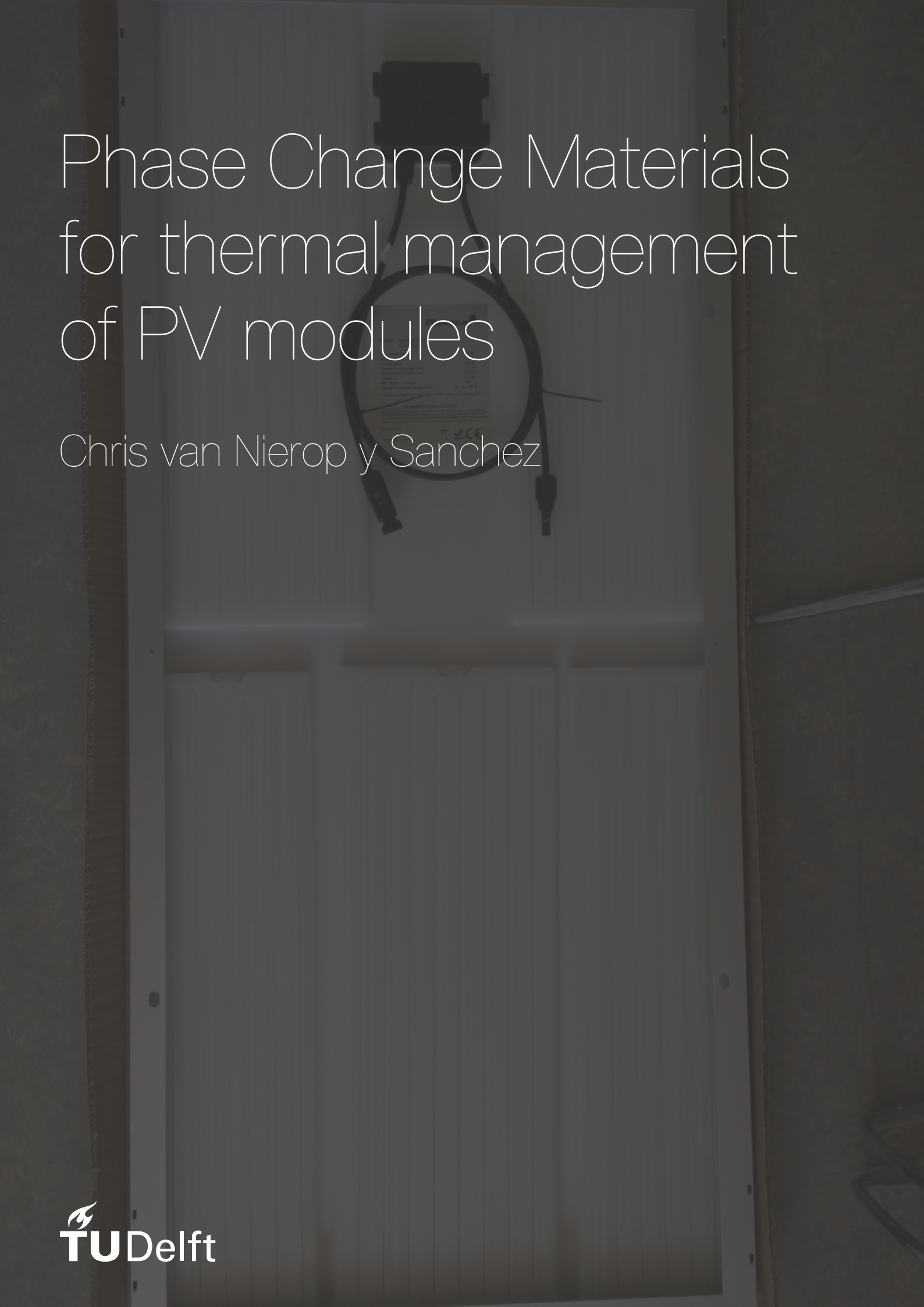

Phase Change Materials for thermal management of PV modules

Chris van Nierop y Sanchez

TU Delft

Phase Change Materials for thermal management of PV modules

by

C. van Nierop y Sanchez

to obtain the degree of Master of Science
at the Delft University of Technology,
to be defended publicly on Friday January 18, 2019 at 14:00 PM.

Student number:	4246209	
Project duration:	January 8, 2018 – January 18, 2019	
Thesis committee:	Dr. ir. Olindo Isabella,	TU Delft
	Prof. Dr. ir. Miro Zeman,	TU Delft
	Prof. ir. Peter Luscuere	TU Delft
	ir. Juan Camilo Ortiz Lizcano	TU Delft

TU Delft

Abstract

Whilst research in solar cell materials lead to higher efficiencies every year, new difficulties arise with every breakthrough to get an even higher efficiency. Therefore, every component of a PV system should be examined, as well as how their behaviour under operation affects performance to improve the overall PV yield. In particular the temperature of a module can have a negative impact on the power output. The drop in power output is a consequence of a negative thermal coefficient that results in a decrease of open circuit voltage with increasing temperature. For silicon solar cells, efficiency drops of 0.4-0.65%/°C have been reported in literature. Moreover, daily repetition of temperature cycles can cause mechanical degradation, thereby decreasing the lifetime of PV modules.

In this thesis, phase change materials (PCM) have been studied as a method to passively reduce the operating temperature of PV modules. This is based on the ability of materials to stay at a relatively stable temperature during a phase change. By placing a PCM at the back of a PV module, the temperature difference between the module and the melting PCM causes a thermal gradient, resulting in conduction of heat away from the module.

In order to find the optimal properties of a PCM, a thermal model was first developed in COMSOL Multiphysics and benchmarked with field measurements from literature. Simulations for Rotterdam, the Netherlands, revealed that an optimized PCM could increase the yearly electrical yield by 1.23% for a rack-mounted module, or 3.52% for a roof-mounted module. Furthermore, measurements were performed with commercially available PCMs under a Large Area Solar Simulator (LASS). These were able to reduce the average module temperature by 30-36°C, albeit under heavy infrared radiation coming from the simulator.

Contents

List of Figures

List of Tables

1 Introduction

1.1. Background

The prosperity and technical development of modern society is based on the capability to convert one form of energy into another for consumption. Therefore, it ensues that energy consumption per capita is largest in wealthy and technologically developed countries. In 2016, energy consumption per capita in the Netherlands was nearly 41 times as high as in Kenya [1]. This quantity of consumption brings about challenges for humankind in the 21st century. First, the current energy infrastructure is highly dependent on fossil fuels, which can be though of as solar energy converted through photosynthesis into chemical energy through millions of years. As humans extract this form of energy at a rate higher than its production, the depletion of fossil fuels seems inevitable in the future. This makes fossil fuels a non-renewable energy source.

A second problem occurs in the form of a supply-demand challenge. The world population is continuously grouwing, and all these new members of society require energy. Furthermore, as living standards are increasing in heavily populated countries like China and India, the energy demand will grow even more. According to the BP Energy Outlook 2035, an increase of 37% in global energy demand is expected. This projected growth is attributed for 96% to non-OECD countries [2]. The depletion of fossil fuels together with the rise in worldwide energy consumption will lead to an imminent increase in price.

A third issue at hand is the bulk of greenhouse gasses released with the burning of fossil fuels. These emissions have increased the atmospheric concentrations of CO_2, CH_4, and NO_x to unprecedented levels, leading to global warming and the acidification of oceans [3].

In order to solve these challenges, it is critical to examine energy sources that will not be depleted and have a low impact on the environment, i.e. renewable and sustainable energy sources. Solar energy, for example, can be converted into electricity with devices based on semiconductor materials. This form of energy conversion is referred to as photovoltaics, and it is becoming a larger part of the energy industry each year. The acknowledgement of its potential by governments around the world has led it to become a fast-growing industry in the energy market [4]. A considerable amount of effort is put into R&D to increase energy conversion efficiency and ultimately decrease the amount of fossil fuels that are used globally.

Whilst research in solar cell materials lead to higher efficiencies every year, new difficulties arise with every breakthrough to get an even higher efficiency. Therefore, every component of a PV system should be examined, as well as how their behaviour under operation affects performance to improve the overall PV yield. In particular the temperature of a module can have a large impact on the power output. Most solar irradiation that reaches the module get converted into thermal energy [5], thereby increasing the temperature, with a detrimental effect on the module efficiency as a result. For silicon solar cells, efficiency drops of 0.4-0.65 %/°C have been reported [6].

1.2. Thermal management of photovoltaic modules

1.2.1. Thermo-mechanical degradation of PV modules

PV modules show mechanical degradation through their lifetime, which can be attributed to the repetition of daily temperature cycles [7, 8]. Figure 1.1 demonstrates 40.7% of PV module failures can be attributed to solar cell interconnection breaking [9], especially due to solder joints that are prone to degradation. The various layers that make up a PV module, illustrated in figure 1.2, have separate thermal expansion coefficients (CTE) that indicate how a material changes in volume with a rising temperature. If one layer expands at a faster rate during the day than the other, it can induce mechanical stress within the other layers. This repetition in thermally induced stress can result in the cracking of the solder joints at first, followed by propagation of these cracks until the PV module fails. Amalu et al. [7] investigated the thermo-mechanical deformation of c-Si PV modules with analytical and simulation methods. It was found that the ethylene vinyl acetate (EVA) is the most prone to thermo-mechanical deformation, followed by the solder which accumulates the most straining.

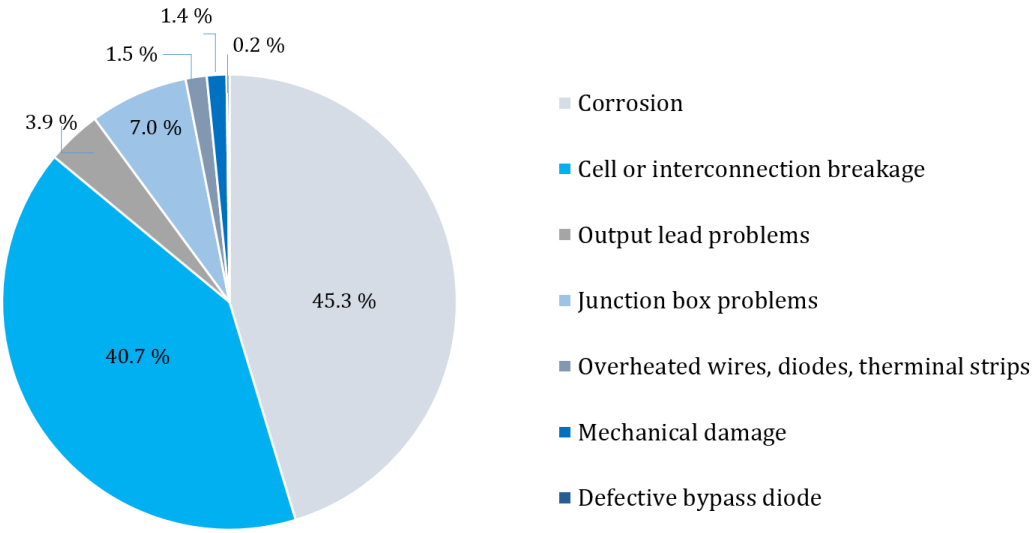

Figure 1.1: Types of field failures observed from 1994 through 2005 at BP Solar and Solarex [9].

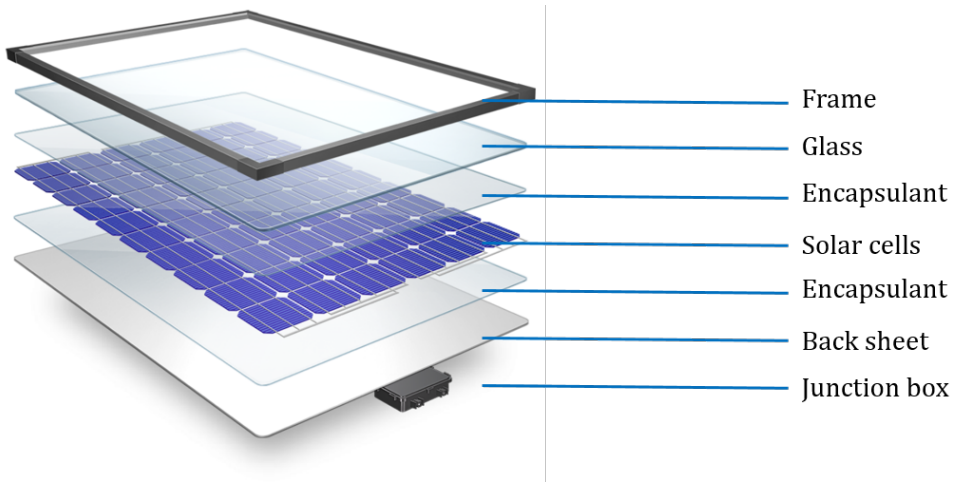

Figure 1.2: Typical structure of a c-Si PV module. Adapted from [10].

1.2.2. Effect of temperature on PV efficiency

An increase in the temperature of a solar module results in a lower conversion efficiency due to a decrease in the maximum power point (MPP) [5]. This parameter is a combination of the fill factor (FF), short circuit current (I_{sc}), and open circuit voltage (V_{oc}):

$$P_{mpp} = I_{mpp} V_{mpp} = FF I_{sc} V_{oc} \tag{1.1}$$

Figure 1.3a demonstrates the temperature dependency of the PV-curve of a silicon solar cell [11]. The MPP can be clearly seen to decrease as the temperature increases, as is the V_{oc}. This is also illustrated in figure 1.3b, showing a clear linear temperature dependence of the open-circuit voltage of a dye-sensitized solar cell (DSSC) [12].

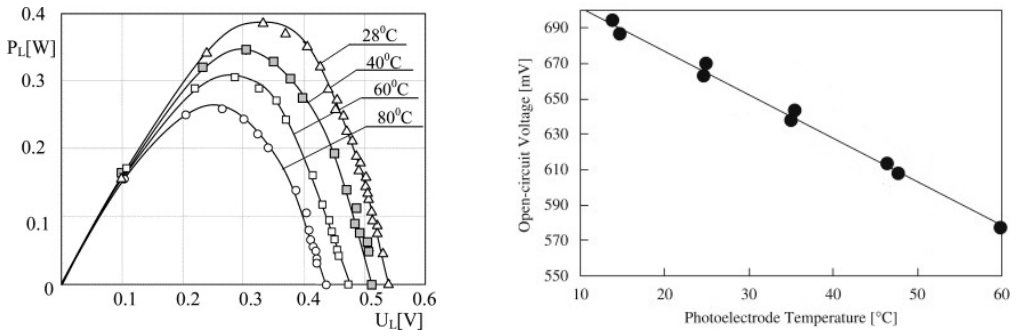

Figure 1.3: (a) Variation of power with voltage of a silicon solar cell [11], (b) temperature dependence of V_{oc} in dye sensitised solar cells [12]

To understand the temperature dependency of V_{oc}, the mathematical relations behind the parameter need to be examined:

$$V_{oc} \approx \frac{nk_BT}{q} ln\Big(\frac{J_{sc}}{J_0}\Big) = \frac{nk_BT}{q}(ln(J_{sc}) - ln(J_0)) \tag{1.2}$$

Where n is the ideality factor of the solar cell, k_B is the Boltzmann constant, T is the solar cell temperature, q is the elementary charge, J_{sc} is the short circuit current density, and J_0 is the saturation current density. J_0 can in turn be defined as:

$$J_0 = BT^{\gamma} exp\Big(-\frac{E_g}{k_BT}\Big) \tag{1.3}$$

Where B is a constant that is essentially assumed independent of the temperature [5], γ is a factor that accounts for possible material-dependent temperature dependencies, and E_g is the bandgap of the absorber material. Combining equations 1.2 and 1.3 results in the following relation:

$$V_{oc} \approx \frac{nk_BT}{q}\Big[ln(J_{sc}) - ln\Big(BT^{\gamma}exp\Big(-\frac{E_g}{k_BT}\Big)\Big)\Big] = \frac{nk_BT}{q}\Big[ln(J_{sc}) - ln(B) - \gamma ln(T) + \frac{E_g}{k_BT}\Big] \tag{1.4}$$

As J_{sc} and B are assumed to have a negligible dependence on the temperature, the temperature-coefficient of the open circuit voltage can be expressed as:

$$\frac{\partial V_{oc}}{\partial T} = \frac{V_{oc}}{T} + \frac{nk_BT}{q}\Big(-\frac{\gamma}{T} - \frac{E_g}{k_BT}\Big) = -\Big(\frac{nV_g - V_{oc}}{T} + \frac{\gamma nk_B}{q}\Big) \tag{1.5}$$

With $V_g = \frac{E_g}{q}$. This coefficient is generally provided in the datasheet of the solar panel by the manufacturer, and can be used to estimate the V_{oc} at varying temperatures:

$$V_{oc}(T_m, G_{STC}) = V_{oc}(STC) + \frac{\partial V_{oc}}{\partial T}(T_m - T_{STC}) \tag{1.6}$$

Where T_m is the module temperature, G_{STC} is the irradiance at standard test conditions (STC) of 1000 W/m^2, and T_{STC} is the module temperature at STC of 25°C.

Most solar cell materials experience a slight increase in short-circuit current at elevated temperatures due to a decrease in bandgap. Although this smaller bandgap results in more charge carriers being generated, its effect on the solar cell efficiency, and therefore its temperature coefficient, is considerably smaller than the temperature dependency of V_{oc}, as can be seen in figure 1.4. The temperature coefficient for the I_{sc} can be found in a solar panel datasheet as well, and can be used to determine the I_{sc} at varying temperatures:

$$I_{sc}(T_m, G_{STC}) = I_{sc}(STC) + \frac{\partial I_{sc}}{\partial T}(T_m - T_{STC}) \tag{1.7}$$

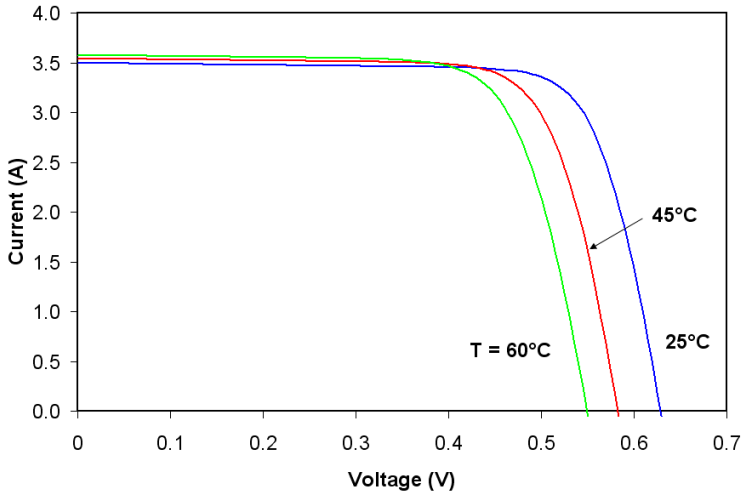

Figure 1.4: Effect of varying temperature on the I-V solar cell characteristics. With an temperature increase of 35°C, the V_{oc} declines by nearly 13%, while the I_{sc} only increases by 2%. Figure adapted from [13].

1.2.3. Thermal management techniques

By understanding the heat transfer mechanisms, methods to remove thermal energy from PV panels can be engineered that are based on one or more of these mechanisms. In these thermal management techniques, an important distinction has to be made between passive and active cooling of the system. The discrepancy is based on whether heat dissipation occurs via natural or forced convection, respectively. While passive cooling does not require additional energy, active cooling is more efficient in thermal management due to a constant renewal of coolant.

One thermal management concept is a *heat spreader*, as shown in figure 1.5. The heat from the PV panel is dissipated through a conductive metal plate with a relative large area compared to the PV panel. Consequently, the plate is cooled via convection through the surrounding air. A large contact area between the plate and the air increases the dissipation, and can be accomplished by the use of fins. This technique was investigated by Araki et al. [14] for concentrated PV with aluminum as the main conducting material, and the temperature rise was only 21°C for a 400x concentrator module.

Another PV cooling method is the *natural ventilated* PV façade system, illustrated in figure 1.6. The approach depends on natural convection to suck cooler air into a vent, thereby cooling the PV panel and exiting through a top vent. The heated air can then be used to heat up the inside of the building as it exits the vents, making it a photovoltaic/thermal (PV/T) hybrid system. Furthermore, radiation from the back of the PV panel warms

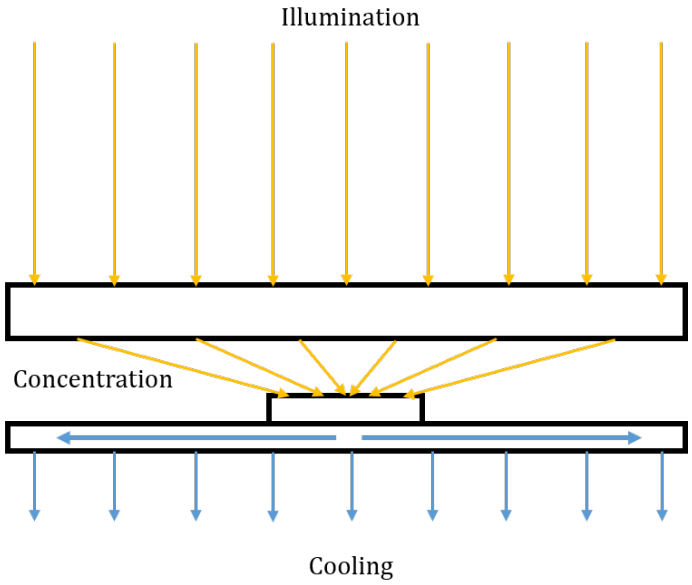

Figure 1.5: Concept of a heat spreader for concentrator photovoltaics, adapted from [14].

the building wall, thus increasing the air circulation by convection. A mathematical model of this type of set-up was verified by Tonui and Tripanagnostopoulos [15]. Additionally, heat can be extracted from the PV panel by *forced ventilation* of air or water, as was investigated by Tripanagnostopoulos in another study [16]. Their set-up can be seen in figure 1.7. The larger volume flow of air increases the heat transfer coefficients, but reduces the net electricity gain due to the use of power to pump the coolant. While the forced ventilated system can be used at any tilt angle, the natural ventilated set-up has an optimal thermal efficiency at 90° [15]. For the water circulated system, heat extraction was found to be more efficient due to a better heat conductivity. Especially in summer, when the temperature of the water supply is lower than the ambient air temperature, the thermal efficiency difference is significant [16].

The contact heat transfer resistance present in the passive and active cooling techniques aforementioned can be eliminated with *liquid immersion cooling* [17]. A dielectric fluid flows over the surfaces of the solar cells, extracting the excessive heat generated by the solar irradiation. When used in a transparent cylindrical vessel, the dielectric liquid can be chosen to have a refractive index that concentrates the irradiation onto the cells, as patented by Russel in 1977 [18]. The patent also mentioned the possibility of fins for additional heat dissipation. Xiang et al. [19] modelled a similar liquid immersion cooling configuration for a cylindrical solar receiver in a dish concentrator photovoltaic system, and found the addition of fins lowered the peak temperature from 61.8^{o}C by an average of 8-10 °C.

The potential of a *heat pipe* to cool down solar cells has likewise been demonstrated to work. A sealed chamber lined with a capillary wick material and working fluid on the inside enables heat extraction with the following mechanism. One end of the heat pipe is heated, which evaporates the working fluid, causing a pressure increase. Consequently, the warm gas diffuses to the cool end of the pipe where it condensates into a liquid again and is drawn back to the heated end of the pipe by the capillary wick. Russel developed and patented the heat pipe for PV applications [20] illustrated in figure 1.8. An internal coolant circuit extracts the thermal energy in this case to ensure a uniform temperature throughout the pipe surface.

A promising cooling strategy is the use of phase change materials (PCM) to keep the PV module at a designed temperature for prolonged periods of time. The thermal energy dissipated by the module is absorbed into the PCM that is chosen to have a suitable melting temperature. By melting, latent heat is stored in the PCM, and the temperature of the materials is relatively stable for the duration of the melting process. Fins play an important role in the transfer of heat in this set-up, as the thermal conductivity of PCM's are generally low. Huang et al. [21] demonstrated that fins significantly reduce the PV temperature, but in result reduce the timeframe of the temperature control as well.

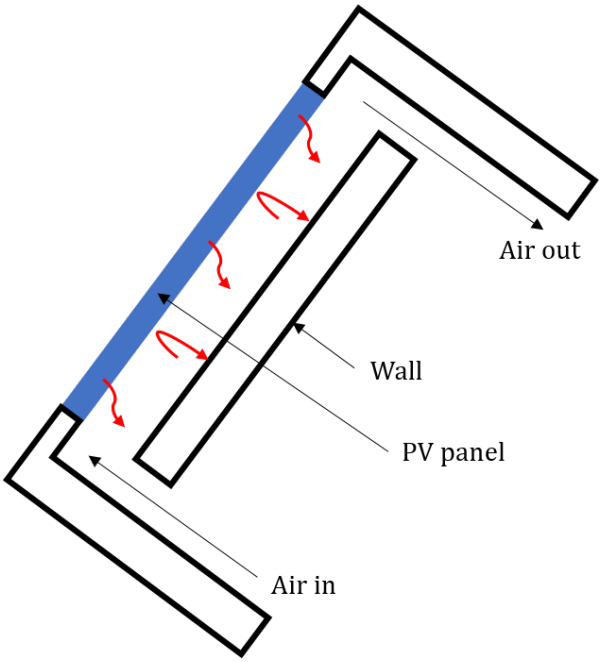

Figure 1.6: Concept of a natural ventilated PV façade system [15]. The PV panel radiates heat to the space behind it and is additionally cooled via convection. Sizes are not to scale.

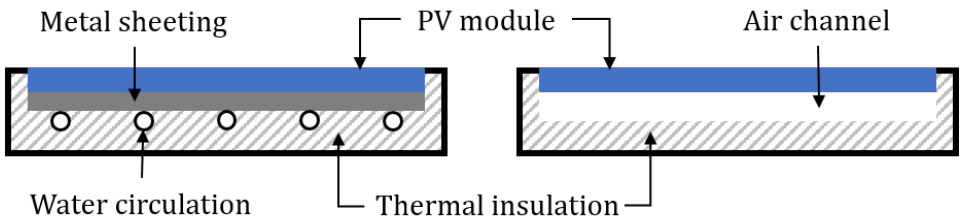

Figure 1.7: Cross section of forced ventilation set-ups with water (left) and air (right) as coolants, adapted from [16].

The section above has identified several thermal management techniques for photovoltaic systems, whose advantages and disadvantages are shown in table 1.1. While fins can be used as a stand-alone cooling technique, they can be used in all the other methods previously mentioned, and are therefore not included in the table. It is clear that PCM can maintain a relatively stable PV temperature without the need for a constant renewal of coolant, thereby not compromising on the added electrical efficiency of the PV system. Its extended heat availability is an added benefit for possible residential BIPV applications, as residential climate control might then also use this heat throughout the afternoon and evening.

Technique	PV temp. regulation	Passive/Active	Thermal storage	Heat availability
Heat spreader	No	Passive	N/A	N/A
Natural air/water convection	No	Passive	Sensible	Immediate
Forced air/water convection	No	Active	Sensible	Immediate
Liquid immersion	No	Active	Sensible	Immediate
Heat pipe	No	Active/Passive	Sensible	Immediate
PCM	Yes	Passive	Latent	Extended

Table 1.1: Techniques for thermal management of PV systems.

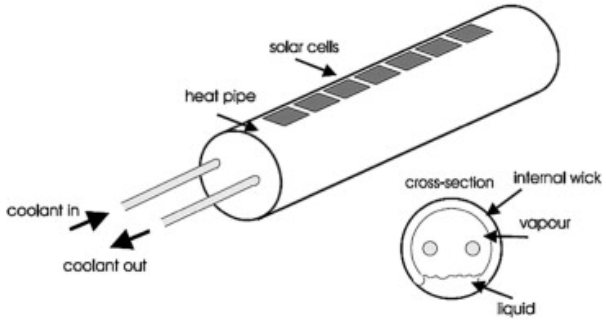

Figure 1.8: Heat pipe intended for uniform thermal management, adapted from [22].

1.3. Phase change materials

In order to apply phase change materials in thermal management systems for PV, it is important to understand the principles of these type of materials. The term *phase change material (PCM)* is used when referring to any substance that is valued for its ability to store and release thermal energy in a phase changing process. This energy is alternatively referred to as *latent heat* and a phase transition has considerable storage capabilities. For example, the amount of energy required to melt 1 kg of ice is the same as the energy required to heat 1 kg of water from 0°C to 80°C. A stable temperature implicates the use of PCM in various types of applications where temperatures need to be regulated, e.g. heat packs, a firefighters' uniform, small electronics, and buildings, as reported by [23] In general, only the solid-liquid phase transition is applicable due to the large thermal expansion of liquid-gas transitions that make it difficult to contain.

1.3.1. Classification

There are more characteristics of phase change materials that require consideration for thermal management and storage. A large latent heat is desired for high heat absorption, and thus heat storage, capabilities. In order to efficiently absorb thermal energy from PV modules a high thermal conductivity is necessary as well. Furthermore, a fixed melting point, i.e. a small temperature interval, prompts consistent phase transitions. Regarding physical properties, a limited difference in density between phases is paramount to ensure the size of the material container is designed appropriately. A large volume expansion can induce mechanical stress and eventually lead to leakage of the container. Another trait to keep in mind concerning the material container is the corrosiveness of the PCM. With respect to other chemical properties, the PCM should be stable to ensure a long lifetime, as well as safe to work with, i.e. non-flammable, toxic or explosive. To ensure economic viability, the PCM should also be widely available and have a low cost.

PCMs can be clustered in various categories depending on their properties, type of phase change, and chemical structure. Figure 1.9 shows an adapted version of the taxonomy of solid-liquid PCMs by Jotshi et al. [24], where materials are first grouped in two main categories relating their phase change: solid-liquid or solid-solid. As the name suggests, solid-liquid materials change phase from a crystalline solid structure to a liquid form, while solid-solid materials remain solid in bulk. Solid-liquid PCMs can be grouped in one of three major classes: inorganic, organic, or eutectics of inorganic and/or organic compounds. Within the inorganic group various types can be distinguished, including salt-hydrates and metallic alloys. For the organic PCMs the major types are paraffins and non-paraffins.

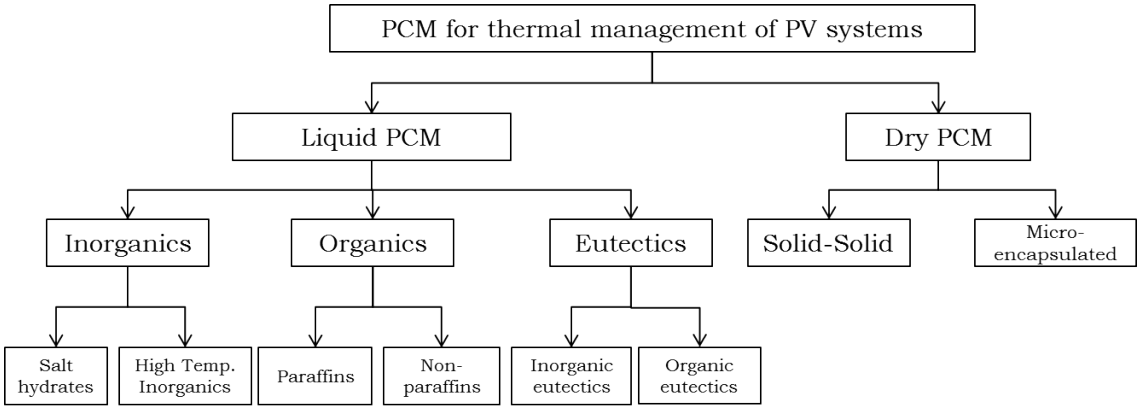

Figure 1.9: PCM taxonomy based on chemical composition. Based on [24]

Salt hydrates are attractive for their relatively high latent heat and high thermal conductivity, resulting in promising storage capabilities, as can be seen from figure 1.10. Furthermore, they experience a small volume change (<1%) during phase change, and are compatible with plastic containers. Disadvantages include corrosiveness, undercooling, loosing water during phase transition, and forming partially hydrated crystals [25].

Although metallic alloys have appealing features like high thermal conductivity and a latent heat higher than hydrocarbons [25], their high density result in heavy systems. Therefore, this type of PCM is not studied for PV/PCM applications.

Paraffins and waxes are a group of saturated hydrocarbon compounds that are a by-product of the oil-industry, but can also be produced synthetically. The most commonly known examples of paraffins are bees wax and candle wax, and they can generally be represented as C_nH_{2n+2} with n being between 20-40. Their have a high potential to be used as PCM for thermal management of PV systems, due to the amount of desirable characteristics. Furthermore, they have a relatively high latent heat and are generally chemically inert, which implies it is neither toxic nor corrosive to its container. Additionally, undercooling is of negligible proportions and there is no phase segregation during the phase change either. However, thermal conductivity of these materials leaves much to be wished for, and their high volume expansion in their phase change (around 10%) can result in leakage of their container [25]. Moreover, paraffins are flammable, and pure paraffins are expensive so only technical grade materials are used to reduce the cost. This lead to a blunt melting point, which affects the consistency in phase change behavior [26].

Non-paraffin organic compounds with the potential to be used as PCMs include fatty acids, esters, sugar alcohols, glycols, and bio-based polymers. While fatty acids have relatively low latent heat, they exhibit excellent melting and solidifying characteristics [25]. Sugar alcohols on the other hand have higher latent heats; however, these compounds may not be expandable for PV systems due to their higher melting temperature.

Eutectics are mixtures of two or more compounds that have definite melting points at specific mixing ratios. Their behaviour is comparable to salt hydrates during phase transition. In literature, mixtures of capric acid and palmatic acid have been studied broadly [27][28][29].

Encapsulating small amounts of PCM composites in polymer shells is an approach to *dry* phase change materials. The polymer capsules range from 10 μm to 1 mm in size with impermeable, semi-rigid walls of < 1 μm thickness. The use of this method results in pockets of air between the granules due to non-optimized packing. This has the downside of reducing thermal conductivity of the bulk layer because contact between the granules is limited. However, volume expansion in the phase transition is decreased as well, as the granules have the capacity to expand.

Using solid-liquid phase change materials is not the only option available for a dry approach. Solid-solid materials are compounds that do not transition from solid to liquid, but instead from one crystalline solid structure to another. Their latent heats are comparable to paraffins and melting temperatures range from

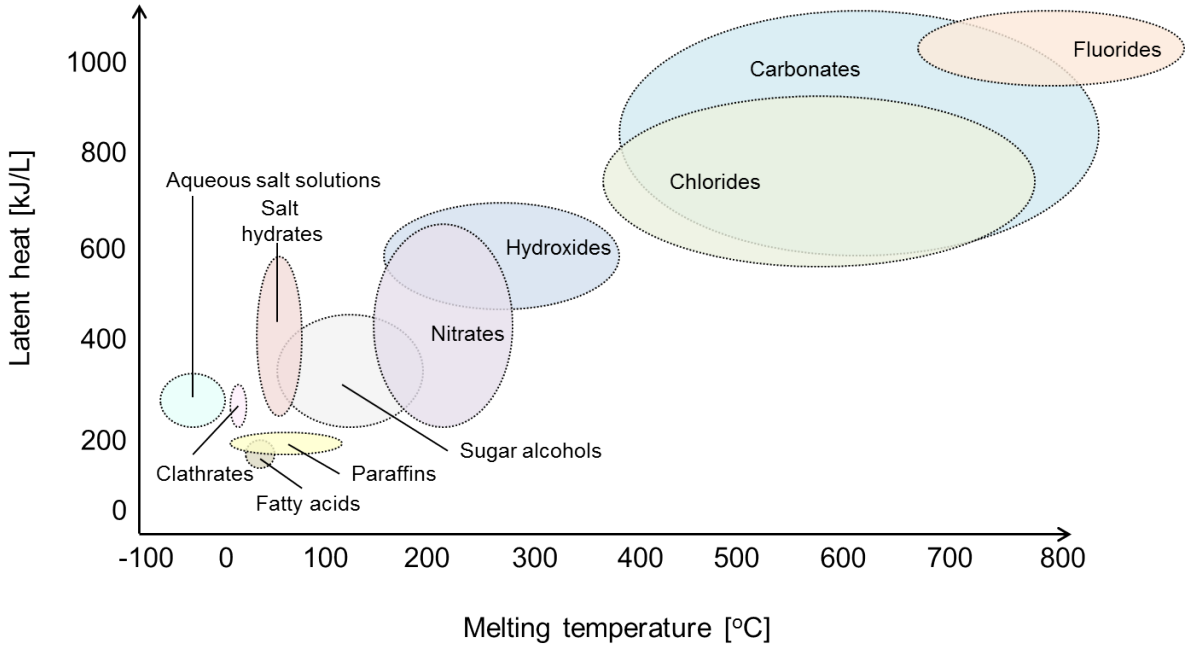

Figure 1.10: PCM classification based on latent heat and melting temperature, based on [30].

ambient to around 100°. Its granular form shows similar disadvantages regarding thermal conductivity as micro-encapsulated PCM.

1.3.2. State-of-the-art PV/PCM systems

Various phase change materials have been investigated for thermal management of PV systems through modeling/simulation studies validated via laboratory of field testing. In 2004, a PV/PCM model was validated by Huang et al. with realistic experimental conditions for the first time [31]. Paraffin wax was simulated as the PCM, and aluminum fins attached to the back of the PV module were used as heat sinks inserted into the PCM to improve thermal conductivity. The validated model was applied to simulate three days with weather data of 21^{st} of June for SE England. It was found that a thickness of 30 mm PCM could lower the peak temperature by 20°C, from 55°C to 35°C. Furthermore, the improvement in thermal performance by the use of aluminum fins was found to be significant. An increased number of fins enables a more uniform temperature distribution within the system; however, it also limits the heat transfer within the PCM by convection.

Hasan et al. studied calcium hexahydrate ($CaCl_2 \cdot 6H_2O$), and a eutectic mixture of capric- and palmatic acid in 2014 [32]. The eutectic mixture was prepared with 75.5 wt% pure capric acid, and 24.8 wt% pure palmatic acid. Both PCMs were stirred for 12 hours at 70°C for uniform distribution of the compounds. The containers of internal dimensions 600 mm × 700 mm × 40 mm were filled with 100 mm of free space left to allow for volume expansion during phase transition. Consequently, the PCM-filled containers were kept at 16°C for 48 hours to allow full solidification before experiments. Experiments were carried out in Ireland and Pakistan with reference PV efficiencies of 10.0% and 13.1, respectively. The capric-palmitic acid mixture was able to reduce the reference temperatures for Ireland and Pakistan by 7°C and 10°C, while for the salt hydrate the PV surface temperature was reduced by 10°C and 21°C, respectively. The electrical yield and heat storage capabilities were found to be significantly higher for $CaCl_2 \cdot 6H_2O$ as well.

The possibilities of petroleum jelly, palm oil, and coconut oil as phase change materials were explored by Indartono et al. [33, 34]. Petroleum jelly is a paraffin mixture of hydrocarbons with a melting temperature range that resulted in a nonconstant temperature profile for the PV/PCM system. The maximum irradiance during the field study was 1120 Wm^{-2}, leading to a maximum temperature on the front surface of the PV module of 60° for the reference system and 54.3°C for the system using petroleum jelly. The average power output of 3.18 W for the reference module was increased to 3.9 W for the PV/PCM system.

In a simulation study, palm oil was identified as a better thermal management option in Indonesia compared to coconut oil due to the average ambient temperature being close to the melting temperature range of coconut oil. For a PCM thickness of 102 mm, palm oil as able to reduce the average temperature of the tested PV module by 9.6°C.

1.4. Objectives and outline of this thesis

Most salt hydrate properties are better suited for thermal management of PV systems compared to organic PCMs, e.g. small volume change in phase transition, high latent heat, high thermal conductivity, and cost. As most of PV applications use modules based on c-Si solar cells, the focus of this work is to study the effect of phase change materials on c-Si PV modules. The objective of this thesis is to reduce the temperature of PV modules, and thereby increasing electrical efficiency of the PV system.

This thesis is divided into six chapters. In this chapter, a background and motivation for this research topic is provided. The effect of temperature on the lifetime and performance of PV modules has been discussed. Additionaly, thermal management techniques studied in literature have been described. In particular phase change materials have been define and classified in the interest of cooling down PV modules.

In chapter 2, the thermal model used in this thesis is introduced. An overview of possible thermal modeling types and heat tranfer mechanisms occuring around a PV module are given. Next follows a detailed explanation of the thermal model used, including its input, the application of PCM, and subsequent benchmarking.

Chapter 3 applies the developed thermal model to examine the influence of meteorological conditions on the ability of a PCM to effectively cool down a PV module. Furthermore, PCM properties are optimized for Rotterdam, the Netherlands.

Chapter 4 concerns the effect of a PCM on the temperature and electrical efficiency of a PV module. An experimental set-up is used to examine the influence of a salt-hydrate on the performance of a module, and these results are compared to the thermal model.

Next, the impact of PCM thermal characteristics on the electrical yield of a module are studied in chapter 5. Consequently, an economic analysis provides the viability of PCMs as a thermal management technique for two sizes of large-scale PV power plants and a residential PV system.

Finally, in chapter 6 the main conclusions of the study are compiled and recommendations for future research are presented.

2

Thermal model

2.1. Overview

As mentioned in the previous chapter, a high temperature has a negative effect on the performance of solar cells. In order to predict the power output of a PV module as a function of its working temperature, as well as the effect of a thermal management technique, it is important to develop an accurate thermal model of the system. Such a model should estimate the temperature of the solar module as a function of meteorological parameters, and in this case, the PCM characteristics correspondingly.

A flowchart of the proposed thermal model is depicted in figure 2.1. As can be seen, the input for the model consists of three main parts. First, solar cell characteristics are used to determine the heat absorbed by the PV module. Consequently, meteorological parameters are introduced to evaluate the heat transfer around the module. In addition, PCM features are included to study the influence of the material on the module temperature. These three segments are assessed in a parallel manner to arrive to the temperature of a module as a function of time. This temperature can in turn be utilized as input itself to determine the efficiency of the module to give the DC power output of a module, but this is left out of the flowchart as it is meant to visualize the thermal model only.

In this chapter, the components of the thermal model are explained. The electrical part of the model is outside the scope of this chapter, but will be treated in chapter 3. In the sections below, the theory behind heat transfer mechanisms is first introduced. Next, a reference model of one PV module is defined based on heat tranfer functions discussed in literature. This input is consequently translated into a 1D heat transfer model in COMSOL Multiphysics, and validated through benchmarking of data found in literature. Afterwards, a layer of PCM is added to the model, and the model is benchmarked with data found in literature again at the end of the chapter.

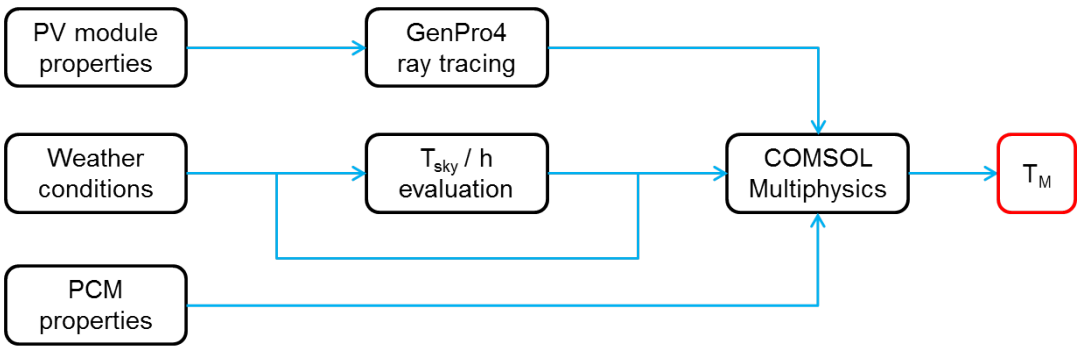

Figure 2.1: Flowchart illustrating the proposed flow of information to compute the temperature of a PV/PCM system.

2.2. Heat transfer in PV modules

2.2.1. Conduction

Heat can be transferred from one body to another through three mechanisms: conduction, convection and radiation. These processes are illustrated schematically in figure 2.2. *Conduction* is the heat transfer from one stationary medium to another as a result of a temperature gradient. When the temperature in a part of the medium increases, the energy content in that part of the lattice increases, giving rise to more vibrations in the structure. These vibrations travel through the lattice, resulting in what is referred to as *conduction*. The transfer of this energy per unit of time per unit of area and can be described by Fouriers law:

$$q''_x = \frac{dQ_{cond}}{Adt} = -k\frac{dT}{dx} \tag{2.1}$$

Where dQ/dt is the heat flow (W), k is the thermal conductivity of the material (W/Km), A is the contact area (m^2), and $\frac{dT}{dx}$ is the thermal gradient through the conducting medium (K/m). This heat flux is directly proportional to the thermal gradient and the thermal conductivity of the material, an intrinsic property of the medium, which represents the thermal resistance of the material.

In a PV module, conduction takes place between its layers. Each layer absorbs a different amount of irradiation from the sun and therefore heats up at a different rate. This induces a temperature gradient, and thus conduction takes place. Additionally, conduction will take place when placing a PCM layer behind the PV panel. Details on the absorbtion per layer and PCM will be further discussed in sections 2.3 and 2.4, respectively.

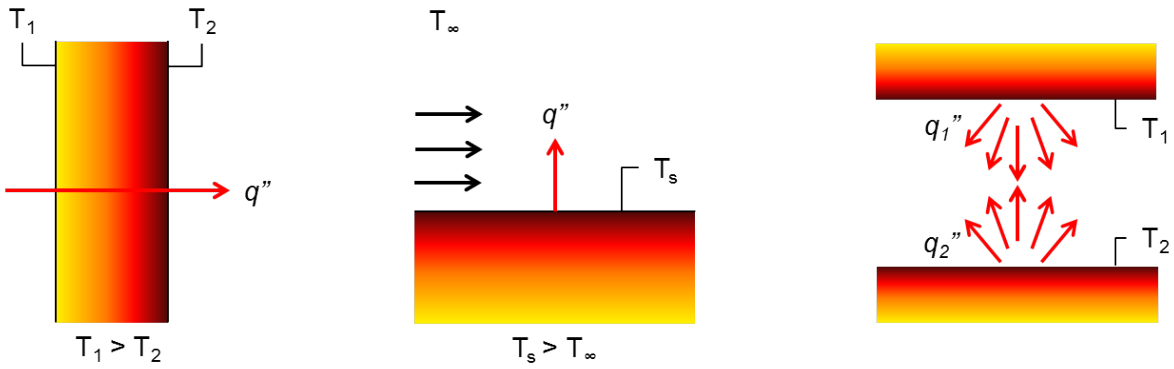

Figure 2.2: Schematic representation of the heat exchange mechanisms. From left to right: conduction, convection, and radiation. Adapted from [35].

2.2.2. Convection

Convection is another form of heat transfer, now caused by the movement of one medium across the surface of another. Similar to the heat flux caused by conduction, the convective heat flux is directly proportional to the temperature difference between the material surface and the fluid flowing. This type of heat tranfer can be described by Newton's cooling law:

$$q''_s = h(T_s - T_{amb}) \tag{2.2}$$

Where h is the heat transfer coefficient (W/m^2K). It is not an intrinsic material property, but rather a variable that depends on parameters such as fluid properties, motion, and surface geometry.

The influence of fluid motion on the heat tranfer coefficient can be allocated to two types of convection, i.e. *forced* and *free* convection. Forced convection implies an external parameter that drives the movement of

the cooling medium, usually a pump or a wind blowing. Natural convection however, is induced by a difference in density caused by temperature gradients. In PV applications, heat removal via convection is generally due to a wind blowing. At higher winds speeds forced convection is dominant, while at low windspeeds free convection plays a larger role in cooling of a PV module.

In literature, experiments in wind tunnels as well as field measurements for various set-ups, e.g. aluminum plates or actual solar panels, have led to correlations to determine h [36]. While some take into account a multiple of geometrical or meteorological parameters, others approximate h as a linear correlation proportional to windspeed alone. For this study, an average heat transfer coefficient was estimated with equation 2.3, where w is the windspeed (m/s). The equation has already been used and validated in literature for a PV/PCM model by Arici et al. [37].

$$h_{air} = 8.91 + 2w \tag{2.3}$$

2.2.3. Radiation

Radiative heat transfer is the third type of heat transfer and in contrast to conduction or convection, it does not require a medium to occur. An object with a temperature above 0 K radiates thermal energy in the form of photons due to electrons falling to the ground state. The sun is an example of a body that radiates heat, which travels through the vacuum of space and eventually reaches the earth's surface. This heat transfer can be described by the Stefan-Bolzmann law [38]:

$$E = \epsilon\sigma\left(T_s^4\right) \tag{2.4}$$

Where ϵ is an emission coefficient dependent on the material surface, σ is the Stefan-Boltzmann constant ($\approx$ 5.670E-8 W/m^2K^4), and T_s is the surface temperature. The coefficient ϵ measures the deviation of the emitting surface from an ideal blackbody, and its value is between 0 and 1. It not only depends on the material, but how the surface is structured as well.

Although a radiating surface might not be in direct contact with other media, these do influence each other. In the case of a PV module, the influence of atmospheric emission onto the module results in a net heat flux:

$$q''_{rad} = \epsilon\sigma\left(T_s^4 - T_{sky}^4\right) \tag{2.5}$$

The sky temperature can be evaluated as a function of the ambient temperature on a clear day [5]:

$$T_{sky} = 0.0552 \cdot T_a^{1.5} \tag{2.6}$$

2.3. Ray tracing

As mentioned in the previous section, each layer of a PV module absorbs a distinct part of the sun's irridiance. By determining these fractions, heat sources within the module can be allocated, and the temperature distribution across these layers can be examined. For this purpose the software *GenPro4* has been used, as it simulates an optical model for solar cells combining wave and ray-optics. In the model, a solar cell is represented as a multilayer structure and calculations are performed to determine the fraction of incident light absorbed in each layer. It has been validated for multiple wafer based and thin film solar cells by Dr. R. Santbergen [39].

2.3.1. Reference absorption layers

Datasheets of PV modules do not provide the specific layers and materials used in solar cells, and therefore a validated reference structure has been chosen from literature, as depicted in figure 2.3 [40]. Its main layers are glass, an encapsulant, a textured solar cell with aluminum back contact, and a back sheet. The reference c-Si layer has an anti-reflective coating and an emitter deposited. The latter is defined by its sheet resistance rather than its actual thickness, as the n-type doping is only higher than the bulk doping concentration in the

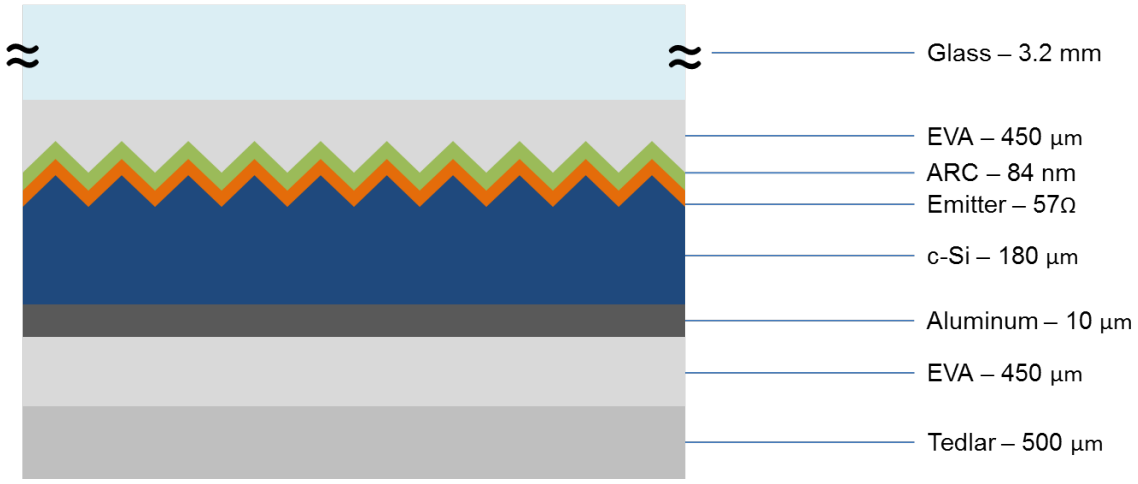

Figure 2.3: Reference module layers used in GenPro4 for optical modeling of reflectance, absorbance, and transmittance of light. Sizes are not to scale.

first nanometers. The *effective emitter thickness* (d_e)is determined by equation 2.7. As the reference emitter has a sheet resistance of 57 Ω, d_e corresponds to 61.4 nm.

$$d_e = \frac{3.5 \mu m \Omega}{R_{sheet}} \tag{2.7}$$

The reference structure was simulated in the wavelength range between 280 and 4000 nm and the results obtained are presented in figure 2.4. Three main absorption areas can be distinguished in the plot. Up to the wavelength corresponding to the bandgap of silicon, approximately 1100 nm, light is mostly absorbed in the silicon bulk. The second main area is between 1100 and 2700 nm, where the photons are predominantly absorbed by the emitter and the back aluminum layer. A phenomenon called *free carrier absorption* occurs at the emitter, where free charge carriers introduced by the doping absorb a photon and are exited to an unoccupied band [41].

From 2700 nm onwards photons have a low energy and are primarely absorbed in the glass layer. As can be seen in the plot, no light is absorbed by the back encapsulant or Tedlar, indicating that the aluminum layer is opaque.

2.3.2. Heat sources

By determining the absorption coefficients of the individual reference layers with ray tracing, the heat sources can be computed. For most components of the solar module structure, the total radiative heat absorbed can be quantified by integrating the product of the absorbtion profile of a layer and the sun's irradiance spectrum:

$$P_{layer}^{HS} = \int_{\lambda_i}^{\lambda_f} A_{layer}(\lambda) \cdot I_{AM1.5G}(\lambda) d\lambda \tag{2.8}$$

This equation is, however, not sufficient for silicon or any layer that converts the radiation into forms of energy other than heat. In the case of silicon, part of the incident radiation is converted into electrical power, and it is therefore necessary to adjust equation 2.8 to take this into account:

$$P_{Si}^{HS} = \int_{\lambda_i}^{\lambda_f} A_{Si}(\lambda) \cdot I_{AM1.5G}(\lambda) \cdot \frac{E_{ph} - E_{gap}}{E_{ph}} d\lambda \tag{2.9}$$

Where E_{ph} is the energy of the incident photon in eV, and E_{gap} is the bandgap of silicon; 1.12 eV at room temperature. This equation is only valid for $E_{ph} > E_{gap}$, as no free energy carriers are generated in the c-Si layer if the photons have an energy lower than the bandgap. However, as losses occur in the solar cell, not all

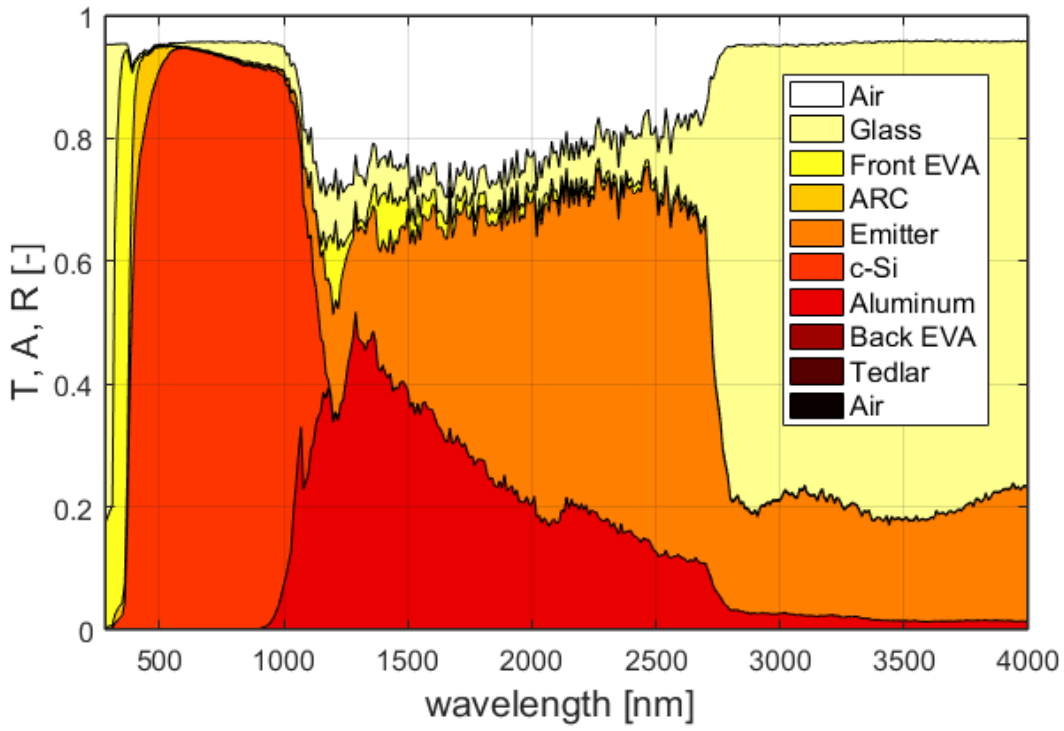

Figure 2.4: Area plot of reflectance, transmittance, and absorbance as a function of wavelength for the layers in the reference structure. Resolution of 10nm.

generated charge carriers are collected at the terminals. These losses contribute to the heating of the module and should thus be considered as well:

$$P_{Si}^{HS} = \int_{\lambda_i}^{\lambda_f} A_{Si}(\lambda) \cdot I_{AM1.5G}(\lambda) \cdot \frac{E_{ph} - E_{gap}}{E_{ph}} d\lambda + (0.42 - \eta) \cdot I_{AM1.5G} \tag{2.10}$$

Where η is the electrical effiency of the PV module as stated in its respective datasheet, and $I_{AM1.5G}$ is the total integrated spectral irracianc of the AM1.5G spectrum (1000 W/m^2). Without considering the losses, η would reach an unrealistic value of around 42%.

Although figure 2.4 shows a large absorption factor for the emitter and glass, the AM1.5G spectrum does not have a high spectral irradiance in those wavelength ranges. Therefore, the absorbed heat in those materials is not high.

2.4. Phase change physics

Heat can be absorbed or removed in two forms; either sensible or latent heat. While absorbing sensible heat results in an increase in temperature for the absorbing body, absorbing latent heat causes a phase change at constant temperature, as illustrated in figure 2.5a. Sensible heat is expressed in equation 2.11 and is a function of the temperature difference between two bodies and mass, while latent heat described in equation 2.12 is only a function of mass. Here, m is the mass (kg), C_p is the heat capacity ($\frac{J}{kgK}$), and L is the specific latent heat ($\frac{J}{kg}$):

$$Q_{sensible} = mC_p(T_2 - T_1) \tag{2.11}$$

$$Q_{latent} = mL \tag{2.12}$$

However, this is only the case for an ideal phase change. In reality, phase change materials are often not

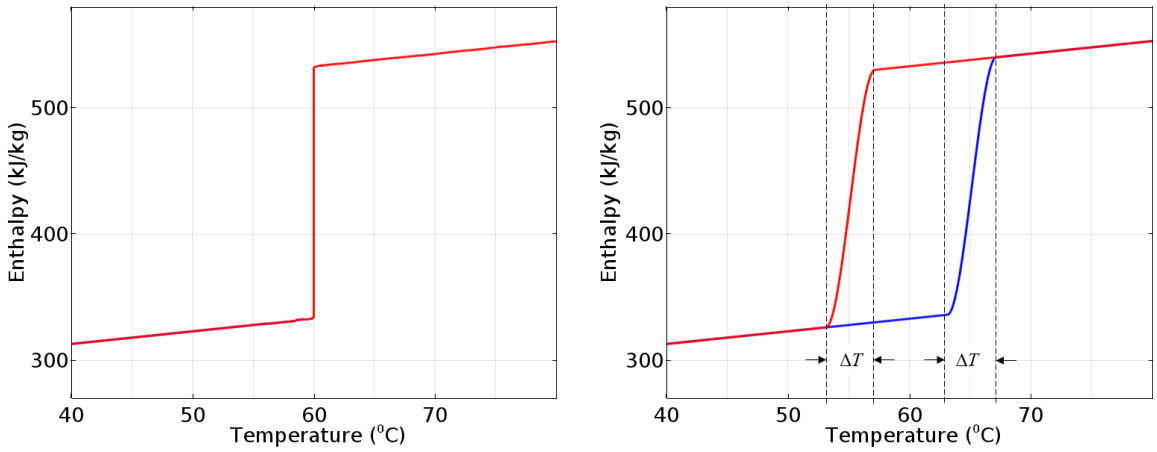

(a) An ideal isothermal phase change without hysteresis. **(b)** A non-isothermal phase change including hysteresis.

Figure 2.5: Enthalpy versus temperature for (a) an ideal phase change, and (b) a realistic phase change, where the blue and red jump in enthalpy represent melting and solidifying due to thermal hysteresis, respectively.

isothermal, meaning that there is a temperature range in which the phase change takes place. This range is larger for impure materials, i.e. mixtures of various composites, and smaller for pure materials. Moreover, thermal hysteresis is involved in the explotation of a PCM's latent heat. This phenomenon is defined as the separation of the melting and crystallization temperature of a material. Hence the phase change occurs at a different temperature depending on its direction, as depicted in figure 2.5b.

2.5. Implementation in COMSOL

2.5.1. Geometry definition

The first process of building the thermal model in COMSOL is defining the geometry. The CAD interface allows for an easy user interface and the tool is notably useful as a complete overlap between geometries is guaranteed. This overlap is important to avoid errors in the mesh generation, which in turn can lead to inaccuracies in simulations. For this study, the layers were build as 1-dimensional structures to reduce computational time when simulating phase change materials. This does not significantly affect the results of the thermal model, as the area of the sides is substantially smaller than the area of the front and back of a PV module. [42]

In literature, a 3D CAD model have been build before to simulate 1D heat transfer by thermally insulating the sides of the model [43]. These studies mostly used a mini-module configuration to reduce computational time in the simulations, while still remaining the option to include the front metal grid for electrical simulations. However, that is of no concern in this thesis and therefore a 1D model is adequate in this case. The resulting geometry as seen in the COMSOL user interface is depicted in figure 2.6

Layer thicknesses from literature were taken as guidelines and applied to the geometries. Similar to standard c-Si PV modules, the structure is comprised of low-iron glass, two EVA sheets, a silicon solar cell, and a Tedlar backsheet to protect the structure. These differ from the reference structure used in GenPro4, as the anti-reflective coating and emitter layer have not been included due to their limited thickness. Instead, the thermal energy they absorb has been added to the heat source corresponding to the silicon bulk layer. Likewise, the silver front grid has not been incorporated due to its minimal thermal resistance.

Once the geometry has been built, material properties can be assigned to the layers in the model. In order to compute heat conduction within the module, the properties required are density (ρ), thermal conductivity (κ), and heat capacity (C_p). For radiative heat transfer, the emissivities (ϵ) of both the front and back surface

Material	Density $[kg/m^3]$	Heat capacity $[J/(kg \cdot K]$	Thermal conductivity $[W/(m \cdot K)]$	Surface emissivity [-]
Glass	3000	500	1.8	0.93
EVA	935	480	0.34	-
Silicon	2329	700	131	-
Aluminum	2700	904	237	-
Tedlar	1200	1250	0.2	0.89

Table 2.1: Material properties of a PV module used in the thermal model.

are necessary. These values were obtained from literature and the COMSOL materials library, and are listed in table 2.1 [40, 43].

The mesh can be generated once both the geometry and the materials have been chosen. A mesh design requires a balance between computational time and accurate results. A coarse mesh reduces the finite elements and therefore less calculations have to run, but this might reduce the overall accuracy of the results. With a fine mesh, it is vice versa. However, in a 1D model the elements are by definition smaller than its 2D or 3D counterparts. Accordingly, a relatively fine mesh of 120 elements along the geometry was deemed sufficient.

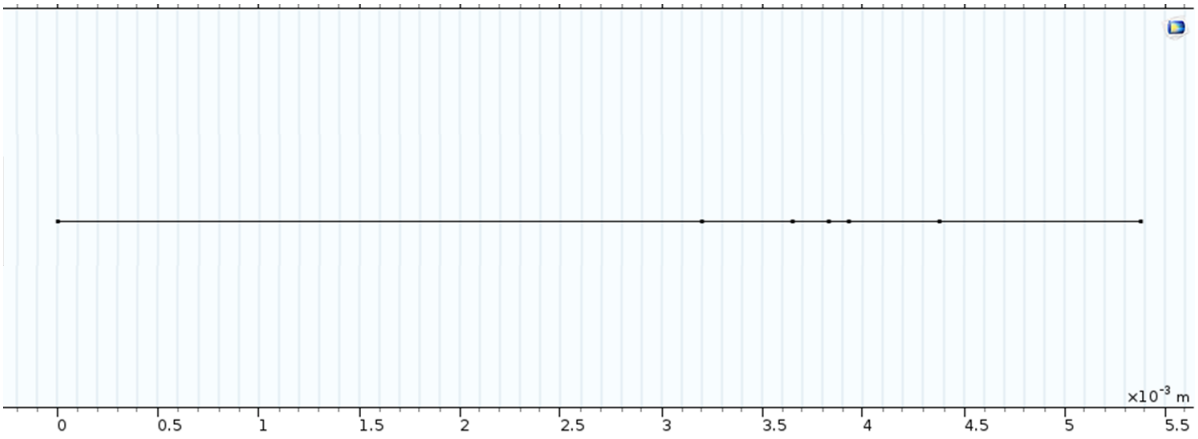

Figure 2.6: 1D layer geometry of a PV module built and simulated in COMSOL. From left to right, the layers between the nodes are glass, EVA, c-Si, aluminium, EVA, Tedlar.

2.5.2. Physics implementation

The last procedure in forming the model is the addition of the chosen physics, initial values, and input parameters, i.e. the weather conditions. The *heat transfer in solids* package in COMSOL allows for all the previously described heat fluxes to be simulated. First, the absorbed irradiance from the sun heats up the layers in the module. These heat up and become heat sources, which conduct thermal energy to their surrounding layers. As the materials properties have already been defined, no extra implementation of conduction is needed. Next, a convective heat flux was added on both ends of the model. The heat transfer coefficient as determined by equation 2.3 was inserted here. Additionally, radiative heat fluxes were included on the same nodes as the convective heat fluxes. The sky temperature was calculated according to equation 2.6.

Addition of a phase change material was likewise possible with the same *heat transfer in solids* package. The following material-specific phase change parameters were defined: the latent heat L, the specific heat Cp, and the initial material state F, which can be either 0 or 1 depending on whether the material is in liquid or solid state, respectively. This last parameter works as a switch for the model to know if it should follow the enthalpy curve for melting or solidification. Other parameters specified are the temperature range over which

the transition takes place ΔT, the median melting temperature T_{melt}, the median crystalization temperature T_{freeze}, and the temperatures at which the phase changes have completed from liquid to solid, T_{top}, or from solid to liquid, T_{bot}, as determined by the following equations:

$$T_{top} = T_{melt} + \tfrac{1}{2}\Delta T \tag{2.13}$$

$$T_{bot} = T_{freeze} - \tfrac{1}{2}\Delta T \tag{2.14}$$

Creating of the enthalpy functions starts by establishing a step function from 0 to 1 to smooth out the curves over the range of ΔT. Consequently, two analytic function were incorporated to simulate the enthalpy curve from solid to liquid and vice versa:

$$H_{S-L} = C_p + L \cdot step(T - T_{melt}) \tag{2.15}$$

$$H_{L-S} = C_p + L \cdot step(T - T_{freeze}) \tag{2.16}$$

The PCM is constructed as a solid within the *Heat Transfer in Solids* package with user defined κ, ρ, and C_p. Depending on the available information on the datasheet of the material, κ and ρ can be either seen as constants or as a variables able to shift from their solid to liquid values. The latter can again be achieved by using a smoothed step function. The specific heat C_p is defined as:

$$C_p = F \cdot \frac{dH_{S-L}}{dT} + (1 - F) \cdot \frac{dH_{L-S}}{dT} \tag{2.17}$$

The differentation operator takes the derivative of two distinct enthalpy functions with respect to temperature, while F defines the material behaviour as either solid or liquid. In order to solve the model and see which enthalpy function should be used, F needs to be evaluated at the previous time step. Therefore, an intial value needs to be defined as well based on the intial surrounding temperature. If the initial temperature is lower than the melting point, the PCM starts in its solid state and F=1. In the case that the initial temperature is higher than the melting point, the PCM starts in its liquid state and F=0. Additional information on the modeling of PCMs can be found here [44].

2.6. Validation

After implementation of all relevant heat transfer physics in the model, field measurement data were used to validate both the PV part, and the PCM integration. It is necessary to validate both in order to compare the temperatures and the influence of the PCM. Meteorological and module temperature data from an outdoor testing facility near Cologne (Germany) was extracted from [40] to validate the PV model. For the PV/PCM model, similar data was extracted for three summer days in Palermo, Italy [42].

Figure 2.7 shows the variation of module temperature as a function of incident irradiation for three different ambient temperatures: 15, 20 and 25 ^{o}C. Furthermore, the two plots represent measurements at (a) 0.25 m/s, and (b) 4.00 m/s. The field measurement are displayed as symbols with error marks, denoting the standard deviation and thus the range in which the simulation results should fall into.

As can be seen, the simulation results indicate a good overall agreement with the field measurements. A linear correlation with increasing irradiation is observed, as reported in literature [5]. For a windspeed of 0.25 m/s, most results fall within the error marks, with the exception at ambient temperatures of 15 and 20 ^{o}C at high irradiances. This might be due to inconsistencies in the in the field measurements or extraction of the data. For the higher windspeed of 4.00 m/s, the simulations seem to follow the general trend of the field measurements better. In this case, the dashed lines are closer to the median measurement data for most conditions.

Weather data for 4-6 September 2010 measured by Brano et al. in Palermo were used as input to validate

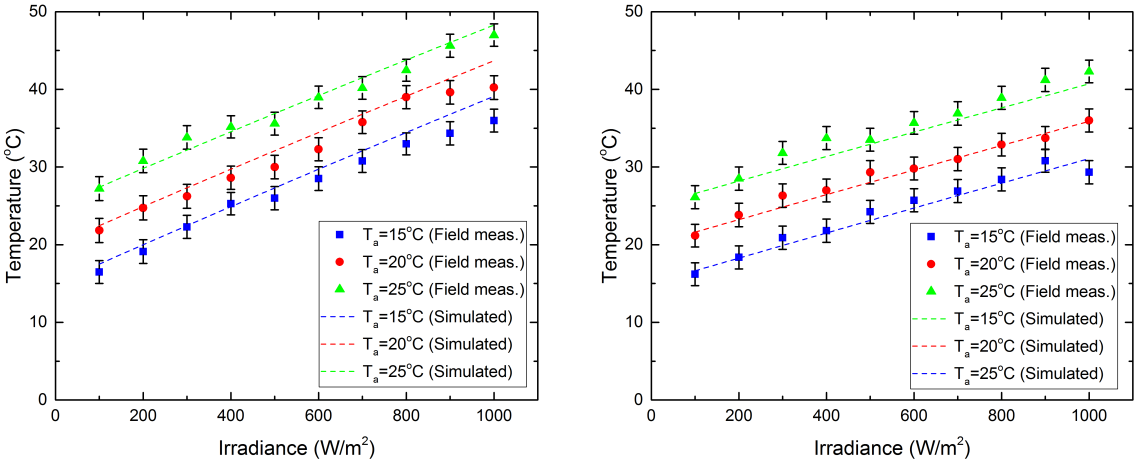

Figure 2.7: Validation of the PV module model created in COMSOL for windspeeds (a) 0.25 m/s and (b) 4.00 m/s. The symbols represent the field measurements, the dashed lines are the simulated results.

the PV/PCM model [42]. The experimental set-up consisted of a 5 cm thick layer of paraffin PCM, encased in a 0.4 mm thick plastic bag. The PCM characteristics are listed in table 2.2. The PV module used in the measurements was a Kyocera KC175GHT-2, with an electrical efficiency of 16%.

The irradiance G_M, ambient temperature T_a, and windspeed w for these three summer days are shown in figure 2.8. As the curves show, the days were nearly cloudless, the ambient temperature increases in the morning and slowly decreases in the afternoon. On the contrary, the windspeeds were higher in the afternoon than in the morning or night.

Figure 2.9 portrays the temperature trend versus time as measured in literature, as well as the results of the thermal model described in this work. The simulations were performed in a 60 second interval. In general, the temperature profiles appear to be similar, reaching nearly the same peak temperatures in the first two days. The largest deviation from the measured values are visible in the late hours of the day, between 18-24 pm. This might be due to a wrong determination of thermal hysteresis parameters of the PCM, especially in the cooling process, e.g. T_{freeze}. These parameters are not readily available in literature and therefore have to be estimated with available information.

In this chapter, a thermal model was created with the software COMSOL Multiphysics to simulate weather conditions and predict the temperature for a PV module with and without a PCM attached onto the back. Although it was possible to match the simulated values to the measured values from literature, it is important for future studies to perform in-house field measurements. Various experimental parameters that can influence heat transfer were not mentioned in literature, e.g. the type of PV mount, height, module tilt. This can result in inaccuracies in the outcome of the simulations, and it is suspected that this is the case for the sole PV module model. In-house measuring of a modules surface temperature with an IR-thermometer during a sunny day revealed a higher temperature than appeared to be possible according to the data in the field study. The next chapter will discuss the experimental set-up developed, which can be a first step in establishing a field study in future research.

PCM Rubitherm no RT-27		
Transition phase	26-28	^{c}C
Solid density	0.87	kg/l
Liquid density	0.75	kg/l
Heat capacity	179	kJ/kg
Specific enthalpy of phase change	1.8-2.4	kJ/kgK
Thermal conductivity	0.2	W/mK

Table 2.2: Thermo-physical characteristics of the PCM used in the validation study.

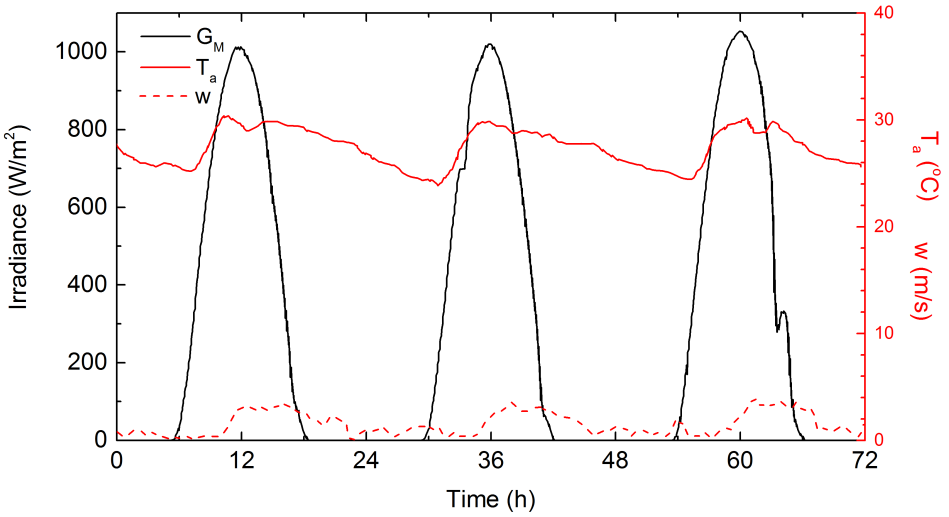

Figure 2.8: Trends of climatic parameters in Palermo (Italy), September 4 to 6. Adapted from [42].

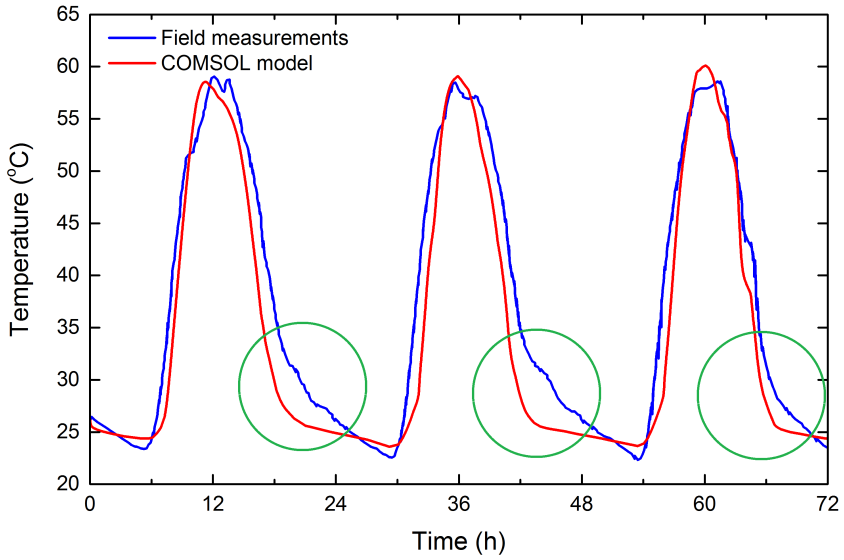

Figure 2.9: Comparison of module temperature between experimental results and the numerical model of this thesis. The green circles mark the time periods in which the deviation is suspected to emerge from incorrect estimation of hysteresis parameters crystalization.

3

Application of the thermal model

3.1. Effect of weather conditions on PCM performance

Once the thermal model previously described was validated, it was further used to simulate a variety of weather conditions. This is important, as the performance of a PV/PCM system depends on both the PCM, as well as the environmental conditions. For example, a PCM with a melting temperature of 20^oC will not give the desired reduction in temperature if the average ambient temperature of a location is 25^oC.

In this section, the PV/PCM system with Rubitherm RT27 as PCM used in the validation of the model is simulated for the duration of one day. The three weather input variables, i.e. irradiance, wind speed, and ambient temperature, were changed to study various weather conditions. The peak irradiance on the PV module was simulated from 100 to 1000 W/m^{-2} in 100 W/m^{-2} intervals, the windspeed from 0 to 7 m/s in 1 m/s intervals, and the ambient temperature from 15 to 30^oC in 5^oC intervals. The peak temperature at the back of the PV module in the PV/PCM system was compared to the peak temperature of a PV module without PCM, resulting in $\Delta T = T_{PV/PCM} - T_{PV}$. The results of these simulations are depicted in figure 3.1.

The first aspect of the results that stands out is the poor performance of the PCM in the simulated conditions with increasing irradiance. In most cases, the peak temperature of the PV module is higher for the PV/PCM system than for the sole PV module, with a positive ΔT as an outcome. This implies that the convection and radiation components of the heat transfer at the back of the module are larger in a sole PV module than the conductive component in a PV/PCM configuration. Improving the heat conduction from PV to PCM by creating a better thermal contact or a PCM with higher thermal conductivity could prevent this detrimental issue, as will be further discussed in the next section.

The correlation between the irradiance and performance of RT27 in this case is the opposite of the desired result. The intention of using a PCM is to reduce the peak PV temperature, which increases with irradiance from the sun. By increasing the rate of thermal energy extraction from the PV module, the peak temperature can be decreased. Analogously, if the rate of thermal energy extraction is decreased, the peak temperature is increased, as is the case in figure 3.1. The wind speed is in turn responsible for fluctuations in convective heat transfer. In locations with higher wind speeds, the peak PV temperature is lower. Overall, however, the employment of this PCM is not beneficial to the peak PV temperature. The wind is able to cool down the PV module more adequate than RT27. Concerning the effect of the ambient temperature, the largest discrepancy occurs when the ambient temperature is higher than the melting temperature of the PCM. At these conditions, the PCM is liquid at the beginning and no longer has the ability to stay at a constant temperature and thus increasing the thermal gradient and thereby the conduction. Instead, it acts as a substantial thermal buffer, making it harder to cool down. The results thus show that RT27 would best be suited for a relatively warm environment with lower irradiances.

It should be noted that the approach taken above is not the optimal means to match a PCM with the location it is best suited for. In reality, weather conditions are not constants throughout the day, while the properties of

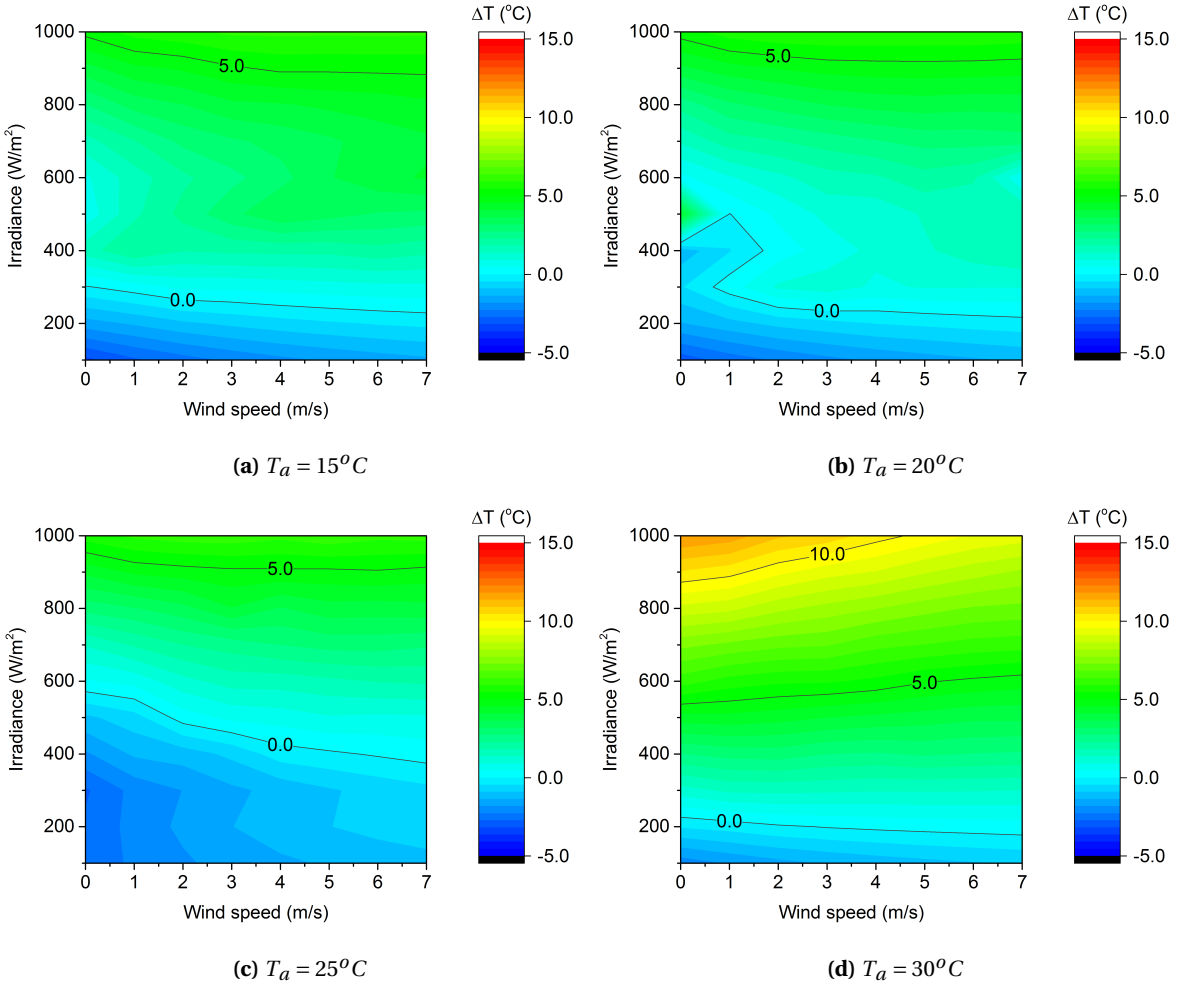

(a) $T_a = 15^oC$ **(b)** $T_a = 20^oC$

(c) $T_a = 25^oC$ **(d)** $T_a = 30^oC$

Figure 3.1: Peak temperature differences of a PV module with and without PCM RT27 for various weather conditions.

a PCM are inherent to the material. Therefore, it is proposed that varying PCM properties in the simulations while using meteorological data of a specific location will yield a better match between locations and PCMs. This will be further discussed in the next section.

3.2. Optimization of PCM properties for the Netherlands

As seen in the previous section, it is important to reflect on the meteorological conditions of a location before deciding on a PCM to use to cool down PV modules. Otherwise, it may occur that the PCM increases the peak PV temperature. In this section, the optimal PCM properties will be studied for Rotterdam, the Netherlands.

3.2.1. Dutch climate

Data on the Dutch climate paramaters were retrieved from the Dutch PV Portal 2.0, a publicly accessible web-page on solar energy in the Netherlands, created by the Photovoltaics Materials and Devices group (PVMD) at Delft University of Technology. The source of the climate data stored in the database is the Royal Netherlands Meteorological Institute (KNMI). It reflects the average meteorological conditions at a location over several decades. The climate data from the PV Portal includes the global horizontal irradiance, diffuse horizontal irradiance, and direct horizontal irradiance. Furthermore, it contains the windspeed measured at a height of

10 m and ambient temperature measured at a height of 1.5 m. For this optimization study, a PV panel facing south is assumed with a tilt of 30^o at a height of 1.5 m, at a location in Rotterdam with no buildings or trees that might cast a shadow on the module. Therefore, a few calculations have to be made before the retrieved data can be used as input in the model.

First, the wind speed measured by the KNMI needs to be adjusted from the reference height of 10 m, to the desired height of 1.5 m. This can be achieved with the logarithmic wind profile law [45] to convert the windspeed at a reference height to the corresponding windspeed at the desired height:

$$U(h_M) = U(h_{ref}) \cdot \frac{ln(\frac{h_M}{z_0})}{ln(\frac{h_{ref}}{z_0})} \tag{3.1}$$

Where U is the wind speed (m/s), h_M and h_{ref} are the module height and reference height (m), repectively, and z_0 refers to the terrain roughness. The terrain roughness is a measure for the average obstacle height in a location and equals roughly 0.03 for an open landscape or 0.4 for an urban environment with numerous high structures [45]. For this study, an open landscape is assumed.

Next, the irradiance incident on the PV module at a tilt of 30^o needs to be determined from the data available in the PV portal database. The parameters available are global horizontal irradiance (GHI), diffuse horizontal irradiance (DHI), direct normal irradiance (DNI), and the altitude (a_S) and azimuth (A_S) of the sun. The irradiance available to the PV module to generate electrical energy consist of three components, as shown in equation 3.2: direct, diffuse, and ground irradiance. The latter signifies the irradiance that is reflected from the ground. Equations 3.3-3.5 display the calculations necessary to determine each of the irradiance components with the available parameters [5].

$$G_M = G_M^{dir} + G_M^{dif} + G_M^{ground} \tag{3.2}$$

$$G_M^{dir} = DNI \cdot cos(\gamma) \tag{3.3}$$

$$G_M^{dif} = DHI \cdot SVF \tag{3.4}$$

$$G_M^{ground} = GHI \cdot \alpha \cdot (1 - SVF) \tag{3.5}$$

Where γ is the angle of incidence (AOI) and SVF is the sky view factor. The factor α is the albedo of the ground surface, in other words the reflection coefficient. For this study, an albedo of 0.1 has been chosen. It should be noted that equation 3.3 is only valid when the sun is above the horizon (a_S>0) and the azimuth of the sun in within 90^o of either side of A_M. Otherwise the value for G_M^{dir} is zero. The cosine of the AOI and SVF can be established as follows [5]:

$$cos(\gamma) = cos(a_M) \cdot cos(a_S) \cdot cos(A_M - A_S) + sin(a_M) \cdot sin(a_S) \tag{3.6}$$

$$SVF = \frac{1 + cos(\theta_M)}{2} \tag{3.7}$$

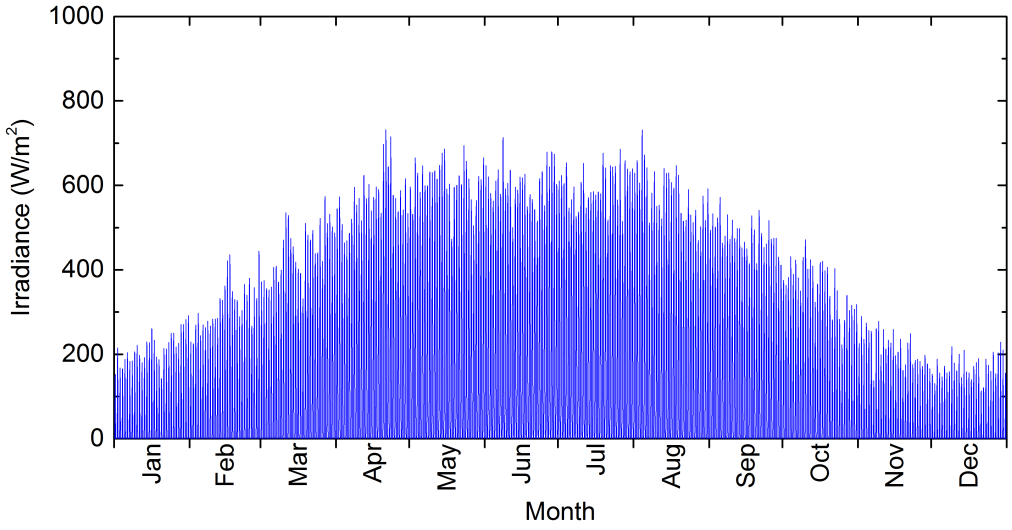

(a)

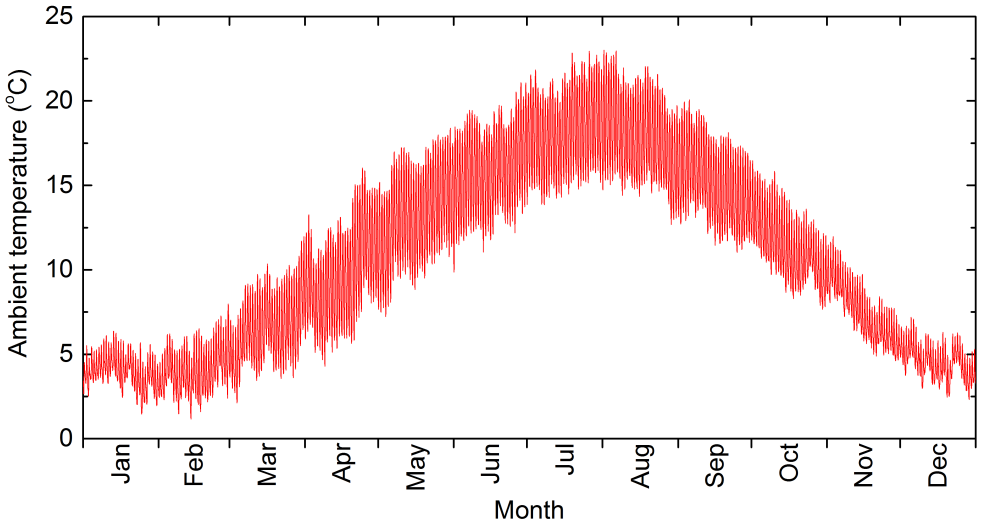

(b)

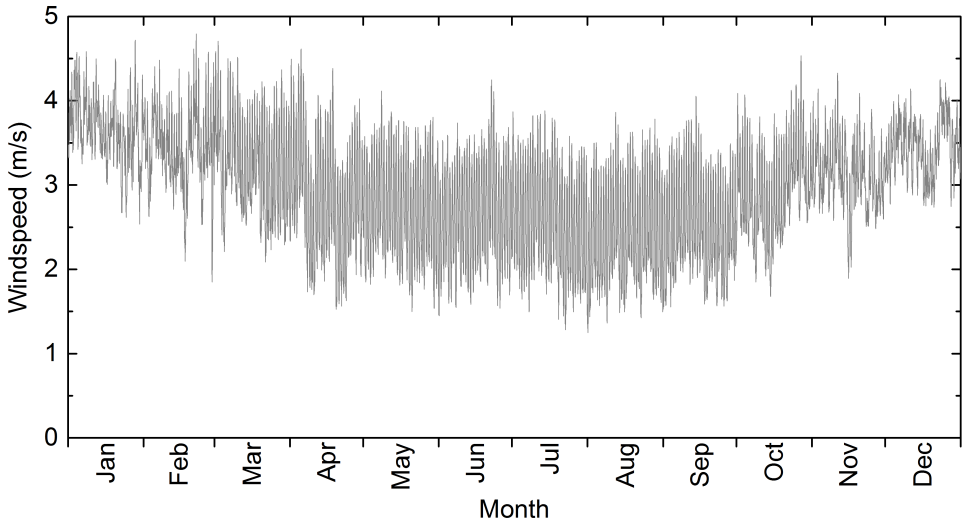

(c)

Figure 3.2: Weather parameters (a) irradiance incident on the PV module, (b) ambient temperature, and (c) windspeed at a height of 1.5m for one average year in Rotterdam, the Netherlands.

With the equations above, the climate data from the PV portal can be adjusted to be used as input in the thermal model. Figure 3.2 shows the three inputs for the model, consisting of data for one year. As discussed in section 3.1, the meteorological parameters influence the workings of a set PCM. Therefore, two distinct days in winter and summer were chosen to study the optimization of PCM properties in Rotterdam, i.e. January 1st and July 1st. This will reveal whether general outcome trends in varying properties are also affected by the weather. The input parameters for the two days are shown in figure 3.3. Although data points were only available for every 30 minutes, the interpolation function in COMSOL allowed simulation for every desired timestep, e.g. in this study 0.01 h.

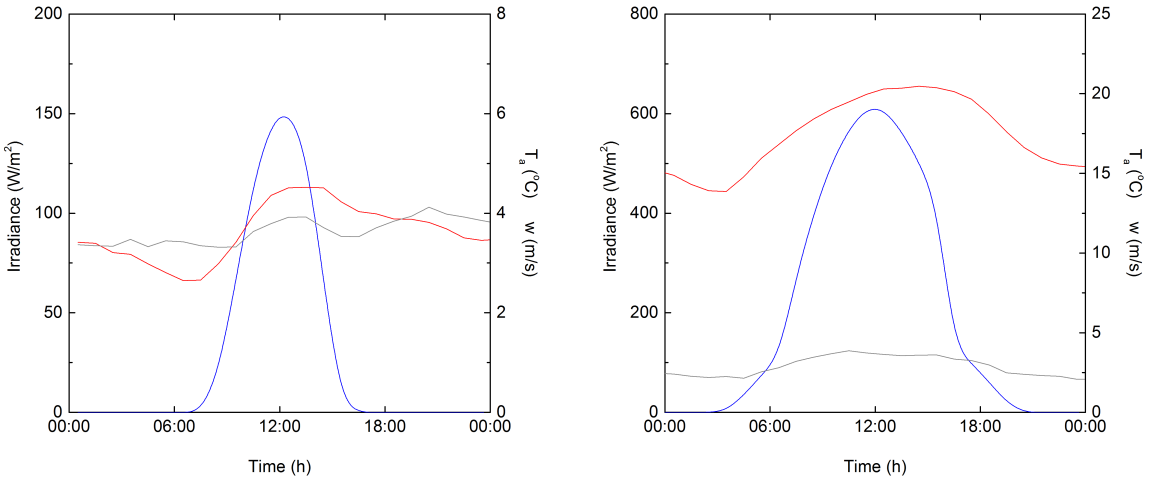

(a) January 1 **(b)** July 1

Figure 3.3: Meteorological input for the thermal model corresponding to (a) the 1st of January, and (b) the 1st of July. The left y-axis shows the irradiance, while the right y-axis displays the temperature and windspeed.

3.2.2. Properties optimization

With the priorly established and validated COMSOL thermal model, and the meteorological parameters for Rotterdam, an optimization study was performed. A reference PCM based on the RT27 was used for the simulations; its properties are presented in table 3.1. The simulations with the reference PCM were carried out for melting temperatures ranging from 0^oC to 40^oC with 1^oC intervals, while the latent heat, thermal conductivity, and thickness of the material were varied to find the maximum reduction in peak PV temperature. The resulting temperatures of the computated PV-PCM system for the assorted PCM properties are presented in figures 3.4-3.6.

As can be seen from figure 3.4, the optimal melting temperature at which the peak PV temperature is the lowest varies, depending on the meteorological conditions, i.e. winter or summer. In both days, there is a certain range of melting temperatures within which the PCM is able to reduce the peak PV temperature. As the latent heat is increased, the peak PV temperature is decreased in both cases, as expected. For January, this decrease seems to saturate at around 200 kJ/kg, with a maximum decrease of 1^oC. Additionally, the change in latent heat does not appear to affect the optimal melting temperature of 4^oC. In July, the decline in peak PV temperature does not saturate within the computated range of latent heats. Furthermore, this decline is coupled with the decrease in optimal melting temperature. As the latent heat increases, the period of time the PCM remains at the melting temperature increases. A lower melting temperature results in a greater thermal gradient, and thus more conductive heat transfer and a lower peak PV temperature. The minimum latent heat for the case of July is 150 kJ/kg.

Reference optimizable PCM		
Transition phase	Variable	^{c}C
Solid density	0.87	kg/l
Liquid density	0.75	kg/l
Heat capacity	200	kJ/kg
Specific enthalpy of phase change	1.8-2.4	kJ/kgK
Thermal conductivity	0.5	W/mK

Table 3.1: Thermo-physical characteristics of the PCM used in the optimization study, based on Rubitherm RT27.

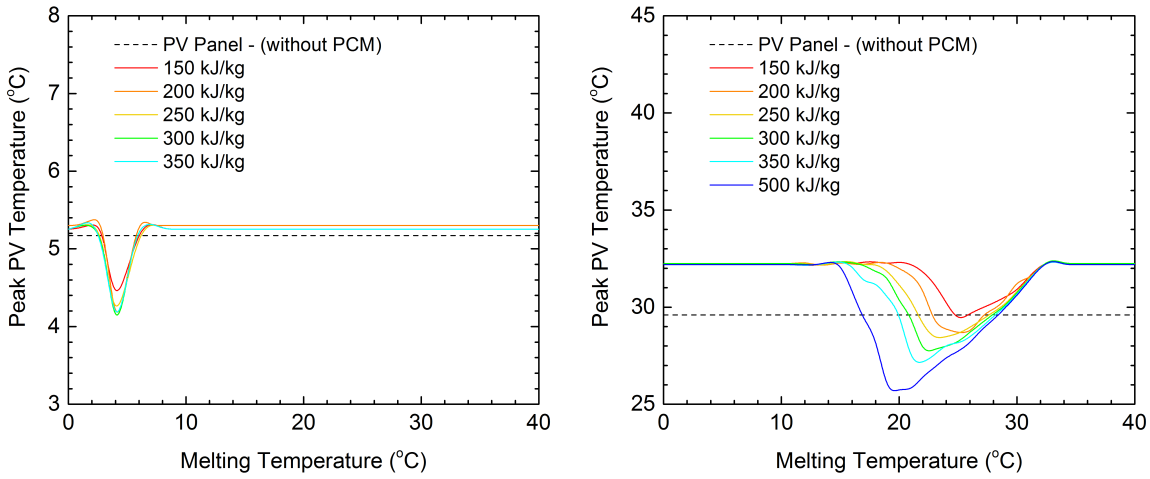

(a) January 1

(b) July 1

Figure 3.4: Trend of peak PV temperatures of the proposed PV-PCM system for various PCM latent heats on (a) January 1st, (b) July 1st.

Figure 3.5 exhibits the outcomes of changing thermal conductivities of the PCM. In January, the narrow range of appropriate melting temperatures remain, and an increase in conductivity slightly decreases the peak PV temperature, but this only differs 0.2^{o}C and saturates at 0.4 W/mK, with a maximum decrease of 1 ^{o}C. The minimum thermal conductivity for the PCM to have a beneficial effect is 0.3 W/mK in July. Overall, the decrease in peak PV temperature is limited, as a higher thermal conductivity reduces the period of time the PCM stays at a fixed temperature. As soon as the PCM reaches it full liquid state, the PV module will increase in temperature at a higher rate again.

Altering the thickness of the PCM layer is the last major parameter influencing the performance of the PV-PCM system. For both weather conditions seen in figure 3.6, the peak PV temperature declines with an expanding PCM thickness. The total latent energy rises, allowing for a longer overall phase transition. Similar to an increase in latent heat, a greater melting period reveals that a lower melting temperature is favorable. The same trends are even more apparent in July, where the optimal melting temperature is 26^{o}C for 10mm, as opposed to 16^{o}C for 50mm.

With the results discussed, optimal properties for a PCM used in Rotterdam can now be proposed. Concerning the choice for thermal conductivity, it will not significantly alter the choice for melting temperature. Therefore, it should be as high as possible to facilitate good heat transfer from the PV panel to the PCM. 0.7 W/mK is an adequate option, as it falls in the range of possibilities for salt hydrate PCMs [46]. The thickness of the PCM-layer is restricted by the weight the mounting structure can hold. However, for the sake of this study no weight restrictions are taken into account; a maximum and ideal thickness of 50 mm is presumed. With regards to the melting temperature, it is clear that its value should be in the range of 15^{o}C-30^{o}C, as opposed

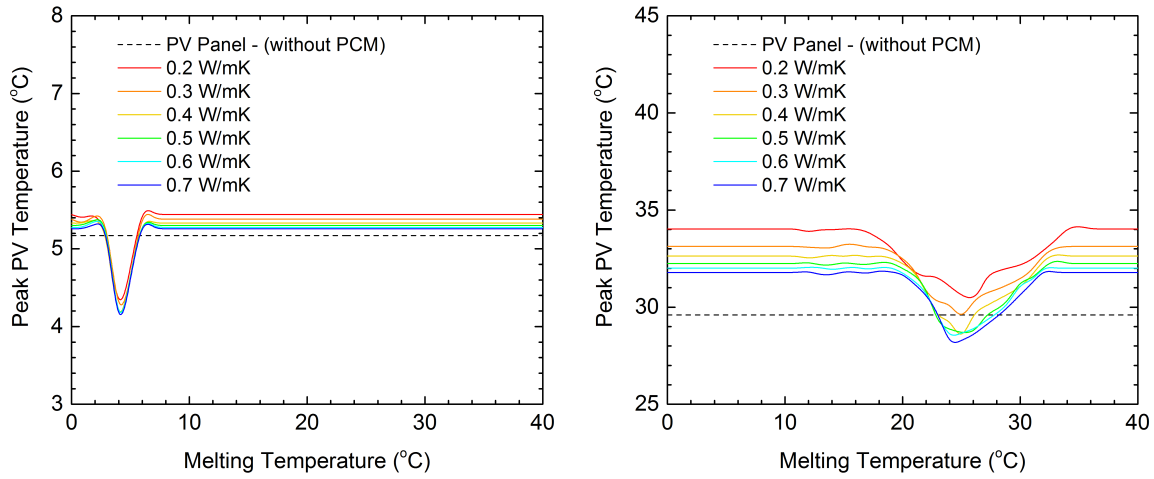

(a) January 1

(b) July 1

Figure 3.5: Trend of peak PV temperatures of the proposed PV-PCM system for various PCM thermal conductivities on (a) January 1st, (b) July 1st.

to lower temperatures, since the peak PV temperature reduction would benefit more in the summer. PCMs with melting temperatures in this range of interest, have a maximum latent heat of 231-296 kJ/kg, depending on the material [47].

With the proposed ideal thermal conductivity, thickness, and latent heat, these values can be put into the thermal model to compute the ideal melting temperature. The outcome can be seen in figure 3.7, with an ideal melting temperature of 16^oC, and a decrease in peak PV temperature of 4.5^oC. Table 3.2 summarizes the proposed PCM properties for Rotterdam.

In this chapter, a method was developed to find the appropriate PCM for different climatic conditions. Optimal PCM properties were identified for Rotterdam, the Netherlands, using weather data of January 1st and July 1st. It should be noted that the peak temperature of a sole PV module in July, 29.6^oC, is lower than expected. This can be attributed to the data used to benchmark the thermal model and, as discussed in 2.6, it is therefore important to perform field measurements in a future study with all experimental parameters identified. Moreover, this proposed method currently takes an extensive amount of time. Automation of this process should also be further studied in the future.

Optimal PCM		
Melting point	16	^{c}C
Solid density	0.87	kg/l
Liquid density	0.75	kg/l
Heat capacity	296	kJ/kg
Specific enthalpy of phase change	1.8-2.4	kJ/kgK
Thermal conductivity	0.7	W/mK

Table 3.2: Thermo-physical characteristics of the proposed optimal PCM for Rotterdam, the Netherlands

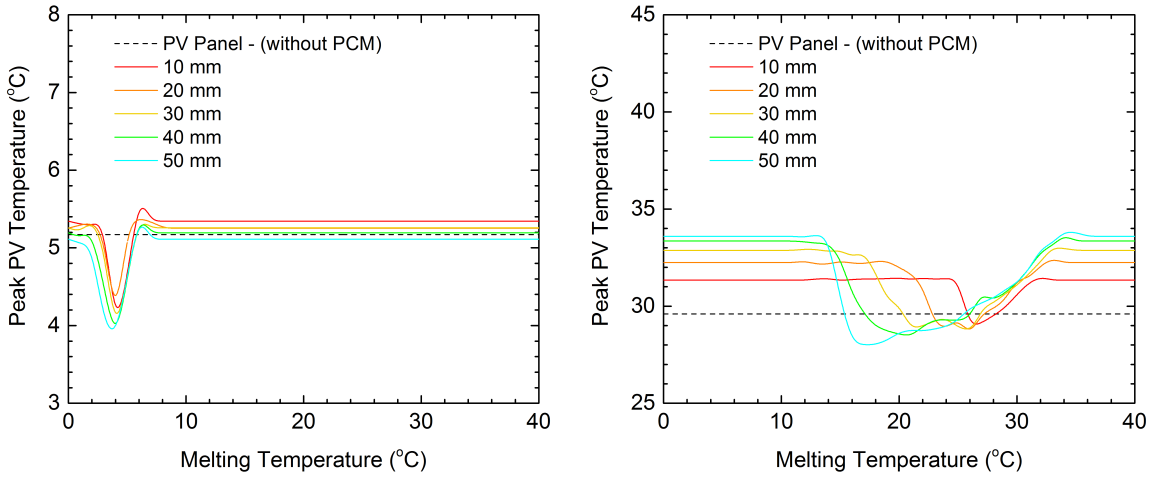

(a) January 1

(b) July 1

Figure 3.6: Trend of peak PV temperatures of the proposed PV-PCM system for various PCM thicknesses on (a) January 1st, (b) July 1st.

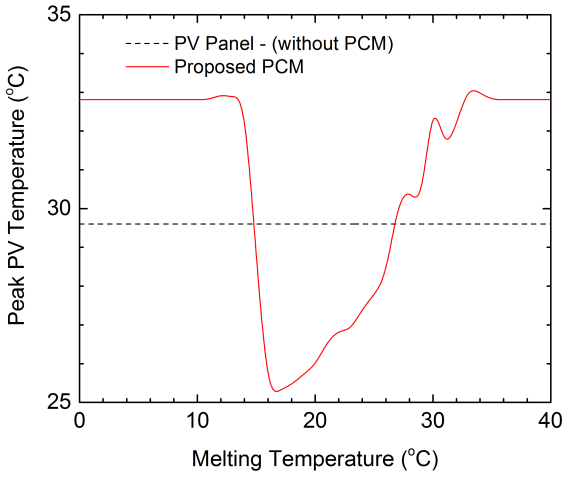

Figure 3.7: Trend of peak PV temperatures of the proposed optimized PCM properties on July 1st.

4

Experimental PV/PCM system

4.1. Experimental set-up

The objective of this section is to describe the techniques and equipment used to measure the influence of PCMs on the temperature of a PV module. The idea is to place a PCM behind a module and measure its IV curves and the temperature distribution on the backsheet of the module as time progresses. A Phaesun Sun Plus 100S monocrystalline silicone module was used for the experiments, as shown in figure 4.2a. It has an electrical efficiency of 15.4% and a power temperature coefficient of -0.45%/^{o}C. Its datasheet can be found in appendix A The module was chosen to have a maximum area coverage with the PCM slabs with fixed sizes.

A Large Area Solar Simulator (LASS), as depicted in figure 4.1, was used. Manufactured by Eternal Sun, it produces class AAA steady-state sunlight, according to the IEC609049:2007. The LASS is also equipped with an IV measurement system. This was used to detect the impact of temperature on the efficiency of the PV module, with or without PCM. A Pico Technology TC-08 datalogger recorded the temperature for eight T-type thermocouples that were attached on the backsheet of the module, according to the lay-out illustrated in figure 4.2b.

The PCMs employed in the set-up were salt-hydrates provided by the company *OC Autarkis* [48]. These were encased in 0.6 mm high density polyethylene (HDPE) with grooves on both sides, as shown in figure 4.2c. HDPE was used as opposed to a metal with a higher heat conductivity to avoid corrosion of the encasing. The purpose of the grooves is to prevent the separation of the salt and water in liquid form, although there is a trade-off in the amount of PCM in the encasing. The PCMs available for the experiments were: Thermusol HD23, HD26, and HD30, with melting temperature ranges of 19-23 ^{o}C, 22-26 ^{o}C, and 26-30^{o}C, respectively. Their characteristics are specified in table 4.1. Working with Thermusol HD23 proved rather difficult as it was melted at room temperature. Therefore, only Thermusol HD26 and HD30 were used in the measurements.

In order to increase the heat flux from the back of the module to the PCM, the set-up was additionaly measured with a layer of thermal paste between the two materials (κ=7.8 W/mK). To maximize the heat conductivity, thermal paste was also applied in the grooves to act as fins. This increases the effective contact area for heat transfer to take place. Aluminum fins have been shown to decrease the module temperature further in literature [21]. A schematic representation is displayed in figure 4.3.

	Components	Latent heat [kJ/kg]	T_{melt} [^{o}C]	ρ [kg/l]	λ [W/mK]
Thermusol HD23	N/A	172	19-23	1.46	0.57
Thermusol HD26	$CaCl_2$ NH_4Cl $SrCl_2$	178	22-26	1.46	0.57
Thermusol HD30	$CaCl_2$ $SrCl_2$	184	26-30	1.46	0.57

Table 4.1: Thermo-physical characteristics of the PCM available for the experimental study. The components of Thermusol HD23 were not available.

Figure 4.1: Large Area Solar Simulator used to determine the influence of the PCM on the PV module temperature. Photograph extracted from [49].

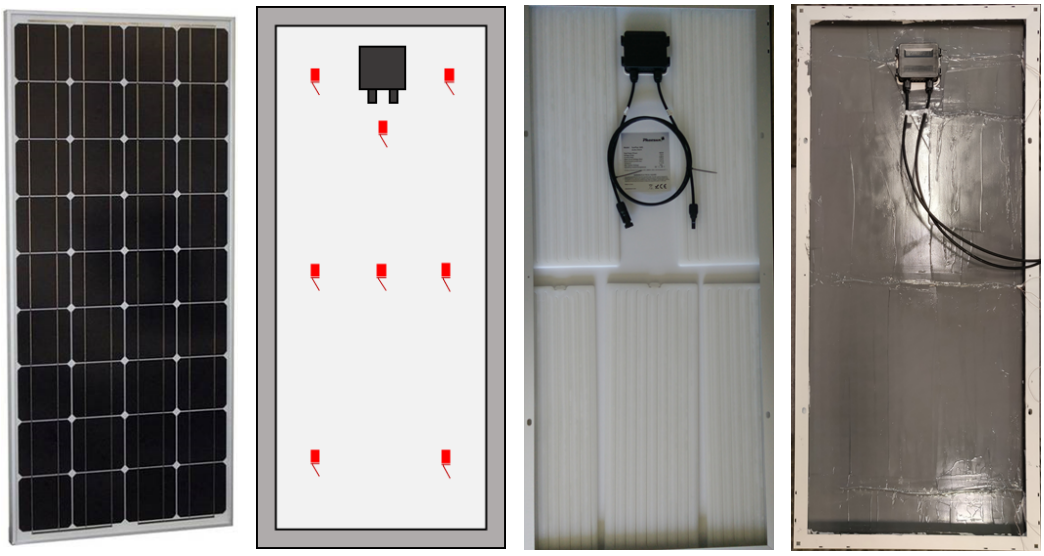

(a) **(b)** **(c)** **(d)**

Figure 4.2: Four depictions of the Phaesun 100S PV module: (a) the front (b) the back with the thermocouple placement shown in red, (c) the placement of the PCM slabs, and (d) the thermal paste applied on the back.

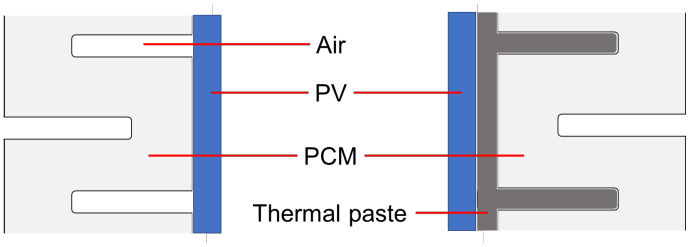

Figure 4.3: Schematic depiction of the PCM placed directly against the back of the module (left), or with a layer of thermal paste in between (right).

4.2. Results

The results in this section illustrate the potential of the measured PCMs in optimal conditions: high irradiance, low windspeed. This results in a high module temperature without the forced convective heat transfer due to wind to cool it down. Therefore, the decrease in module temperature and increase in its electrical efficiency was expected to be highest for these conditions when using a PCM.

Figure 4.4a and 4.4b depict the IV and PV curves of the Phaesun PV module for increasing temperatures. As can be seen, an increase in temperature has a detrimental effect on the V_{oc}. A slight increase in I_{sc} can be observed as well, although the overall consequence is a decrease in power output. The maximum power point (MPP) declines from 96 W at 28^{o}C, to 77 W at 71^{o}C.

The phase change for both PCMs has been examined by exposing a PCM slab with the irradiance of the LASS. Thermocouples were attached at the front and back of a PCM, with the front thermocouples covered with cardboard to insulate them from direct irradiance, which might affect the measurements. It is important to note that the thermocouples are measuring the temperature of the HDPE encasing, not the PCM itself. Therefore, it is possible that through the flow of the melted of the PCM an air bubble was situated beneath the thermocouple, thereby influencing the measurement. To negate this issue, the average of the three thermocouples on each surface was taken.

The development of the temperature over time for the PCMs is exhibited in figure 4.5. The T vs time curve for the PV module is additionally given as a reference; the measurement was stopped at around 16 minutes to prevent the module from getting damaged. An initial sharp increase in temperature is observed for the front side of both PCM slabs during the first two minutes, associated with the increase of temperature of the HDPE by the irradiance. Consequently, the temperatures rise in a moderate trend as the PCM absorbs latent heat. On the backside, the temperature of HD26 remains nearly constant value for 13 minutes, after which all of the PCM has melted and its temperature rises. For HD30, the backside temperature slowly increases by 4^{o}C during the first 19 minutes, which might indicate an evident ΔT. In any case, the significantly slower rate at which the PCM reaches high temperatures suggests they can help decrease the temperature of the PV module with proper thermal contact is made.

In figure 4.6a, the temperature progression over time is illustrated for all configurations. As can be seen, a sole PV module heats up rapidly when exposed with the irradiance of the LASS. After nearly 16 minutes, measurements had to be stopped to prevent any damages to the module. Both PCMs are clearly able to slow the heating of the module. As parts of the backsheet were not covered with PCM, hotspots were created causing non-uniform temperature distribution across the surface. Therefore measurements had to be stopped before the PCMs were completely melted to prevent any damage to the module.

The trends in electrical efficiency (η) for the configuration can likewise be seen in figure 4.6b. As expected, their values drop significantly over time with the sole PV module seeing the largest difference over time since η is inversely proportional to the temperature. Accordingly, a PCM covered module has a lower decline in η.

Figure 4.7 exhibits the measured IV curves with increasing temperatures, as well as the progression of said temperature for the areas of the module that were covered and uncovered with PCM. In the latter, the refer-

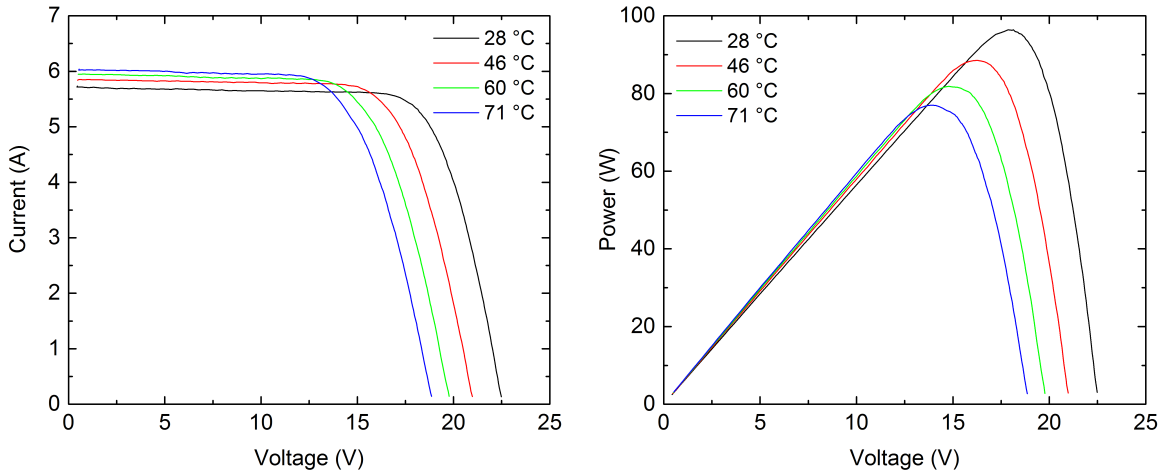

(a) **(b)**

Figure 4.4: IV and PV curves for the Phaesun solar module for increasing temperatures.

ence PV module was added for comparison. The temperatures shown in the IV curves are the average values of the thermocouples located on areas covered by the PCM. At first inspection, the PV/PCM system seems to behave similar to the sole PV module; as its temperature increases, the V_{oc} decreases significantly while the I_{sc} slightly increases. However, there are noticeable steps in the IV curves at higher temperatures. These will further discussed below.

The measurement with HD26 was stopped at around 16 minutes to prevent the uncovered module from reaching a higher temperature. However, for the last measurement, with HD30, it was decided to stop the procedure at 30 minutes. In these additional minutes of measuring, the temperature of both areas only increased by 8^oC, indicating the system was reaching towards steady state. There is no clear indication in the curves of the completion of phase change of the material, therefore it is important to note that a full area coverage is desired to continue measurements for prolongued periods of time.

The T vs time curves reveal a large difference in temperature between the area covered with PCM and the areas without. This phenomenon can be explained by looking at the temperature curves measured. The uncovered area of the module follows a nearly identical path compared to the sole PV with a slight offset that is suspected to occur due to a difference in initial temperature. On the other hand, the temperature of the PCM-covered area increases at a considerably lower rate, leading to a temperature difference of up to 30^oC for HD26 and 32^oC for HD30.

This large temperature difference results several solar cells to perform worse than the PCM-covered counterparts, causing mismatch losses. Generally, mismatch losses occur when part of a module is shaded or by the interconnection of solar cells without identical properties. Accordingly, the electrical parameters of one or more solar cells are significantly shifted compared to the remaining devices. As the I_{sc} of the hot solar cells becomes larger than the relatively cool cells, a current mismatch occurs. Likewise, a voltage mismatch arises as the V_{oc} of the hot solar cells drops substantially. It is suspected that these mismatches are the cause of the steps in the I-V curves. Therefore, it is once again important for future studies to achieve a full coverage of the back of the PV module with the PCM.

Figure 4.8 shows the results of applying thermal paste between the module and the PCM to increase thermal contact and thermal conductivity. The whole back area of the module was covered with thermal paste, as opposed to the PCM. This was implemented in an attempt to reduce the difference in temperature between the PCM-covered area and the uncovered area, with the thermal paste acting as a heat spreader discussed in 1.2.3. This was not achieved, as can be seen in figures 4.8b and 4.8d. The temperature of the uncovered areas increased at a higher rate than the sole PV, resulting in again a relatively short measurement.

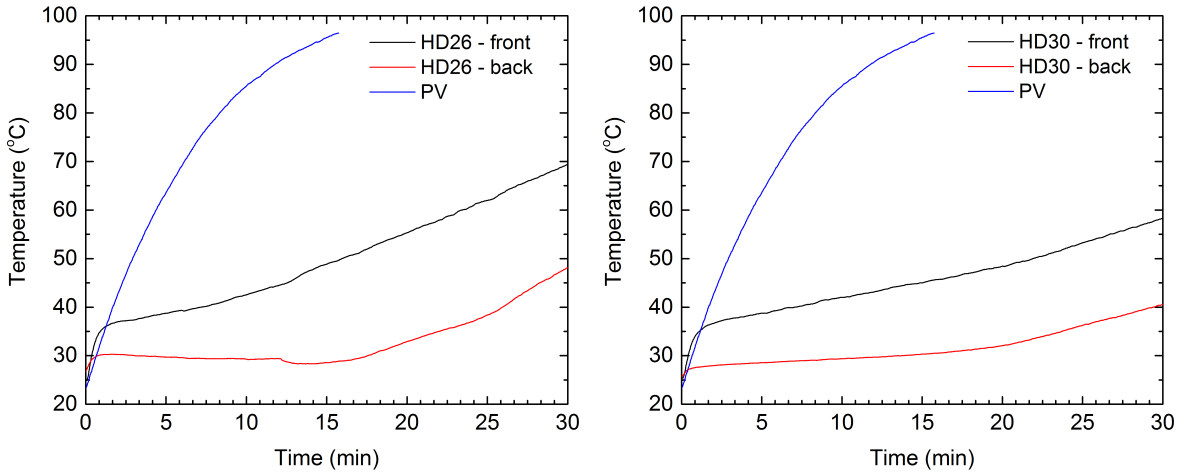

Figure 4.5: Progression of temperature for PCMs (a) HD26 and (b) HD30 measured under the LASS. The temperature curve for a PV module is shown for reference.

The other function of the thermal paste, i.e. creating a better thermal contact between the PV and the PCM and conducting thermal energy from the PV to the PCM at a higher rate, was effective. Compared to the sole PV module, the PV/PCM system with thermal paste was able to reduce the temperature of the module by 36.1^{o}C and 32.9^{o}C using HD26 and HD30, respectively. This variation in outcome can be attributed to the difference in melting temperature of the PCMs.

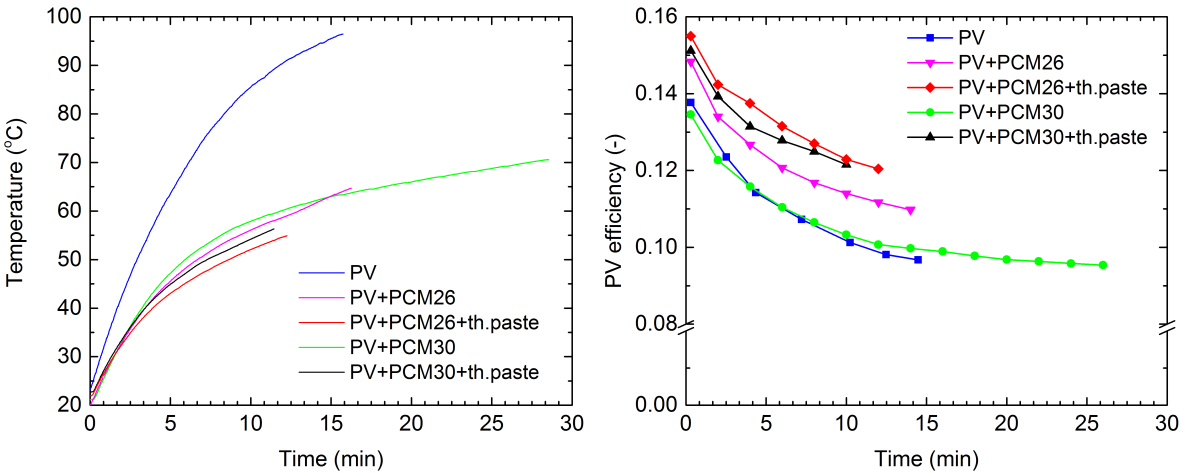

Figure 4.6: (a) T vs time for the averaged PCM-covered thermocouple values, (b) η vs time for the various configurations.

4.3. Modeling of experimental conditions

With the measurements discussed above, it has become clear that the experimental set-up built had short-

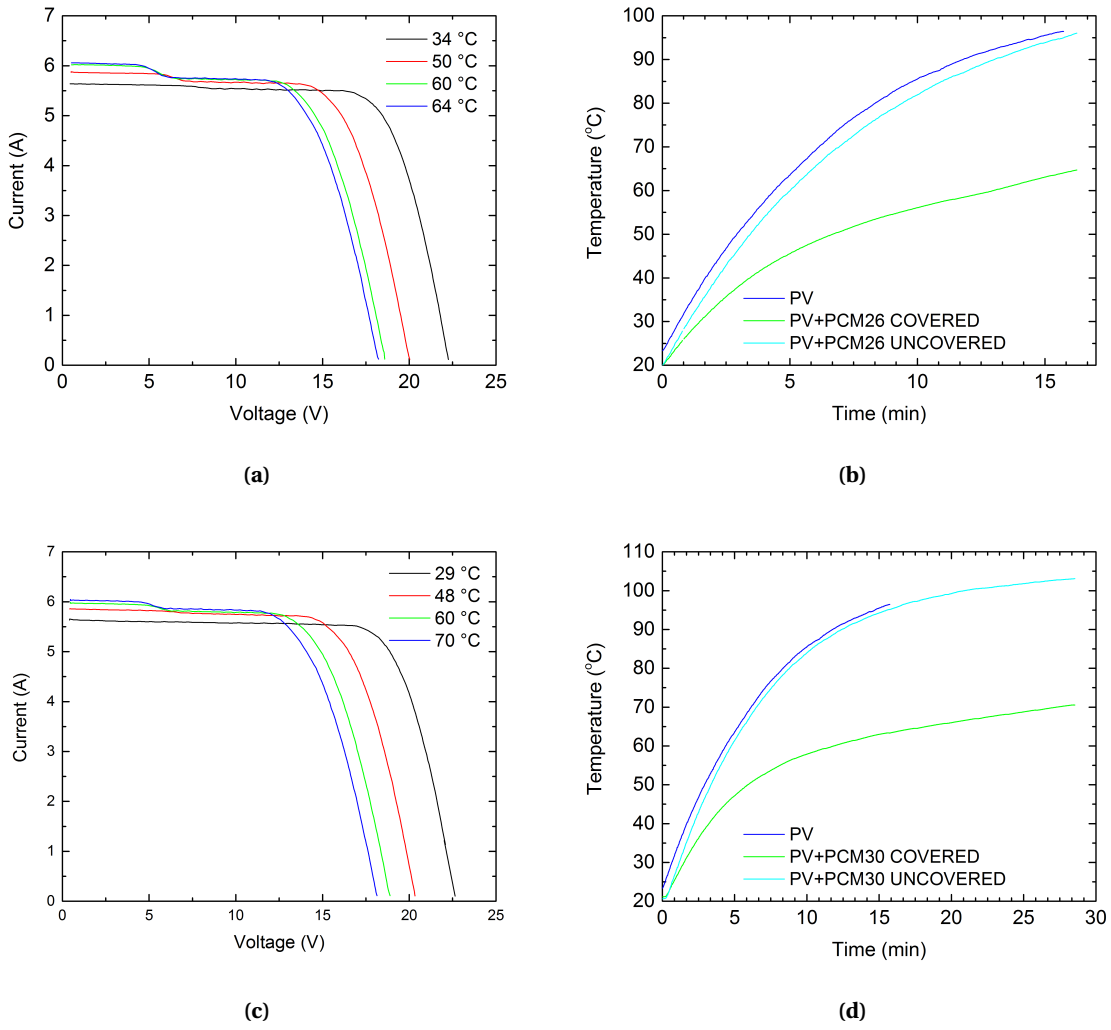

Figure 4.7: IV curves (left) and temperature curves (right) for the Phaesun solar module with with PCMs HD26 (a-b) and HD30 (c-d) without a layer of thermal paste. Steps in the I-V curves are visible around 6V for higher temperatures.

comings. Especially the coverage of the PCM and the contact between the material and the PV module are considered to have a disadvantageous effect on the performance of the system. In order to check the temperature trend if these shortcomings were to be eliminated, the PV-PCM configuration parameters were introduced into the thermal model.

With that, several assumptions had to be made due to a lack of data. First, it was presumed that the absorbance for the irradiation from the LASS is the same as for the AM1.5 spectrum. The spectral irradiance data for the LASS is only available until 1050 nm. Therefore, the absorpion behaviour cannot be predicted. A comparison of the AM1.5 spectrum and the available data for the LASS can be found in appendix B. Another assumption was that the PCM slabs used had no grooves, therefore creating more contact area with the PV module. Moreover, a constant ambient temperature and and evenly distributed thermal paste layer of 1mm were presumed. The results of these simulations are shown in figure 4.9.

The curves clearly exhibit a more effective reduction in temperature than the experiments, with a temperature below 50^oC for all configurations after 30 minutes. Additionally, the temperature of PV-HD26 becomes higher than the PV-HD30 configuration in both the experiment and the simulation, albeit with a time delay. Furthermore, a significant reduction in temperature is achieved with the inclusion of the thermal paste; for both PCMs, this decrease amounts to around 11^oC.

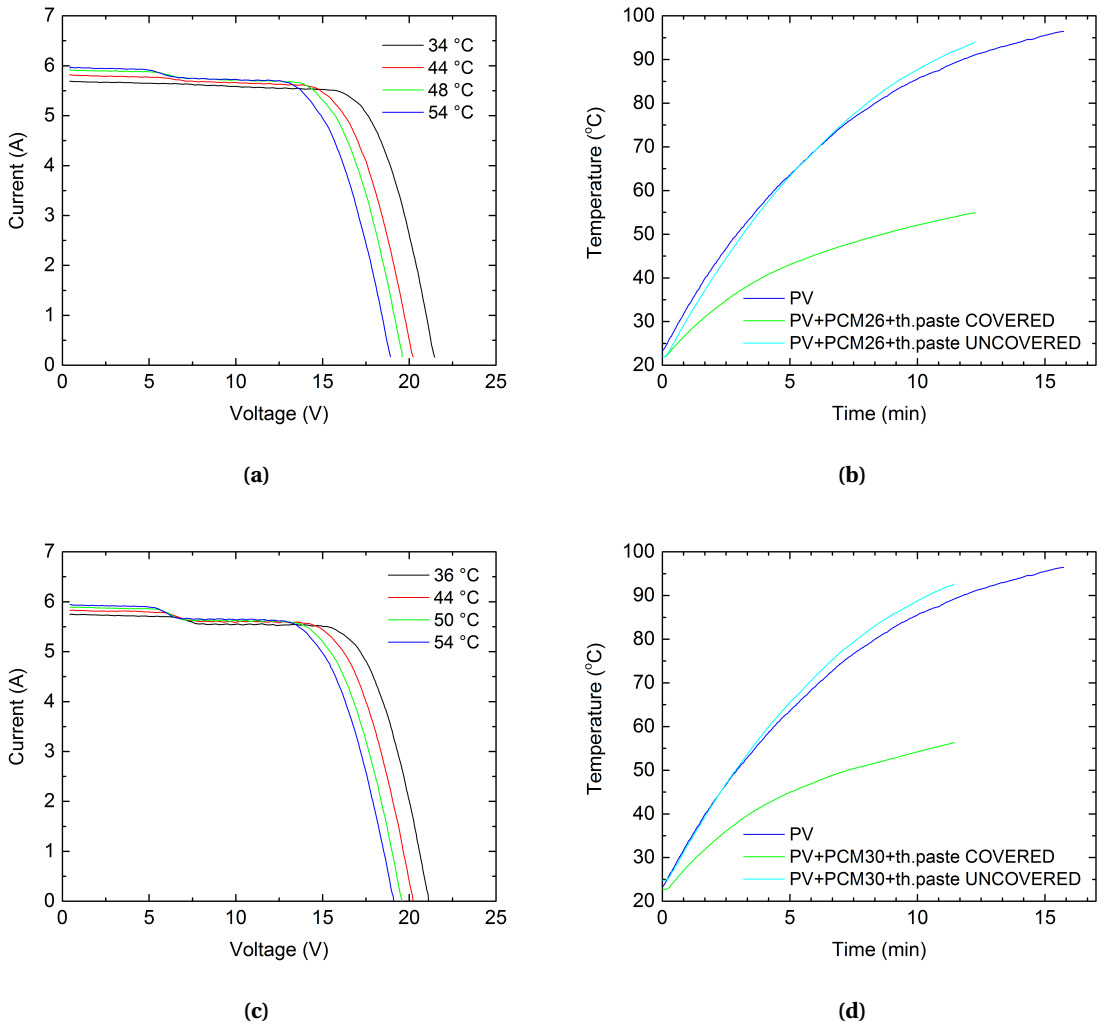

Figure 4.8: IV curves (left) and temperature curves (right) for the Phaesun solar module with with PCMs HD26 (a-b) and HD30 (c-d) including a layer of thermal paste. Steps in the I-V curves are visible around 6V for higher temperatures.

These simulations do certainly not reflect the actual circumstances of the experiments due to the assumptions made, but they do make clear that the PCMs have more potential if the hurdles of the current experimental set-up are overcome.

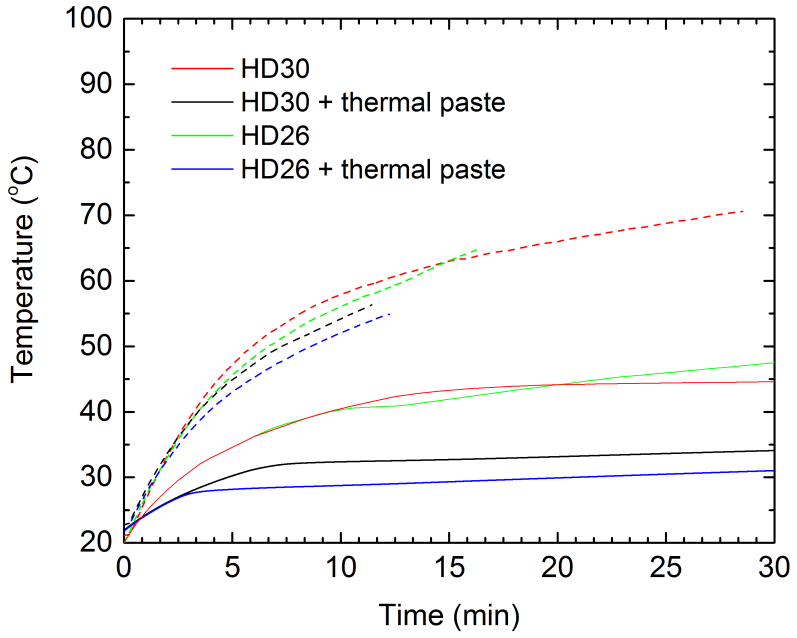

Figure 4.9: T vs time for the averaged PCM-covered thermocouple values (dashed lines), and the simulated values (straight lines).

5

Significance of the PV-PCM system

In the preceding chapters, the optimal PCM was computated for Rotterdam, and a PV-PCM system was builded and tested. This chapter will consider the significance of such a system, e.g. the difference in power produced by a PV module, and the economic viability for a PV-PCM system in the Netherlands.

5.1. Potential benefits on the power production

5.1.1. Electrical yield analysis

The optimal PCM for Rotterdam has been proposed, and two existing PCMs have been studied. Now, their potential benefits can be discussed. The performance of a PV module with and without PCM has been simulated for each month to examine the performance increase. To achieve this, the V_{OC}, I_{SC}, P_{MPP}, and η were first determined as a function of irradiance at 25^oC [5]:

$$V_{OC}(25^oC, G_M) = V_{OC}(STC) + \frac{nk_BT_{STC}}{q} \cdot ln(\frac{G_M}{G_{STC}}) \tag{5.1}$$

$$I_{SC}(25^oC, G_M) = I_{SC}(STC) \cdot \frac{G_M}{G_{STC}} \tag{5.2}$$

$$P_{MPP}(25^oC, G_M) = FF \cdot V_{OC}(25^oC, G_M) \cdot I_{SC}(25^oC, G_M) \tag{5.3}$$

$$\eta(25^oC, G_M) = \frac{P_{MPP}(25^oC, G_M)}{G_M A_M} \tag{5.4}$$

Where n is a diode quality factor set to 1.5 [5], and A_M is the module surface area. By combining the equations above, and the temperature coefficient κ found in the PV module datasheet, the PV temperatures that resulted from the computations can be used to determine the electrical efficiency per timestep [5]:

$$\eta(T_M, G_M) = \eta(25^oC, G_M) \cdot [1 + k(T_M - T_{STC})] \tag{5.5}$$

Integrating the product of the irradiance and efficiency over the desired time period results in the DC electrical yield of the PV module. Simulations were performed for two different types of PV mounting structures. First, a rack mounting structure with free flow of air at the back of the PV module that allows convective heat transfer on both sides. Second, a PV module on a tilted roof of a well-insulated house, allowing for no convective or conductive heat transfer at the back of the PV module or PCM. Both modules were set at an angle of 30^o, and no buildings or landscape were assumed to cast shadows for the module to receive the same amount of irradiation. Examples of the two simulated configurations are displayed in figure 5.1.

(a)

(b)

Figure 5.1: Examples of the types of PV module mounts simulated: (a) rack mount [50], (b) roof mount [51].

5.1.2. Rack-mounted module

Figure 5.2 shows the total DC yields per month for a rack-mounted Phaesun Sun Plus 100 S with and without four types of PCM: the optimized PCM determined in chapter 3, and the three commercially available PCM Thermusol HD23, HD26, and HD30. The first thing that can be noticed is that the difference in energy production is marginal for all PCMs. The change in yield caused by the optimized PCM ranges from -0.52% in March, to a maximum +2.30% in July and August. As the total yield is already higher in summer due to higher irradiances, a negative effect on the PV performance in colder months is condoned. All together, this results in a yearly increase of 1.41 kWh electrical power, which amounts to 1.23%. The benefits are significantly lower for the commercially available PCMs. Over a whole year, HD23, HD26, and HD30 can potentially alter the PV module output by 0.09%, -0.10%, and -0.31%, respecively. The electrical yield and effect of the PCMs per month and the whole year are listed in table 5.1.

Rack-mounted PV module									
	PV Electrical Yield [kWh]					**Difference PV - PV/PCM [%]**			
	No PCM	Optimal PCM	HD23	HD26	HD30	Optimal PCM	HD23	HD26	HD30
January	3.49	3.49	3.49	3.49	3.49	-0.03	-0.09	-0.07	-0.07
February	5.37	5.36	5.36	5.36	5.36	-0.11	-0.08	-0.08	-0.08
March	9.63	9.58	9.60	9.60	9.60	-0.52	-0.26	-0.27	-0.27
April	13.31	13.40	13.25	13.26	13.26	0.63	-0.45	-0.41	-0.41
May	15.33	15.56	15.34	15.28	15.26	1.51	0.09	-0.34	-0.45
June	14.70	14.99	14.78	14.69	14.64	1.94	0.55	-0.08	-0.40
July	15.20	15.55	15.25	15.25	15.16	2.30	0.33	0.32	-0.28
August	13.74	14.05	13.81	13.78	13.70	2.30	0.51	0.34	-0.30
September	10.31	10.49	10.31	10.27	10.27	1.67	-0.04	-0.39	-0.38
October	7.14	7.16	7.12	7.12	7.12	0.31	-0.22	-0.22	-0.22
November	3.50	3.50	3.50	3.50	3.50	0.04	0.01	0.01	0.01
December	2.58	2.58	2.58	2.58	2.58	0.08	-0.04	-0.04	-0.04
Total year	**114.29**	**115.70**	**114.40**	**114.18**	**113.94**	**1.23**	**0.09**	**-0.10**	**-0.31**

Table 5.1: Monthly and annual values for the DC side yield of a rack-mounted PV module and 4 types of PCM configurations, and the change in yield relative to the sole PV module. Location: Rotterdam, the Netherlands.

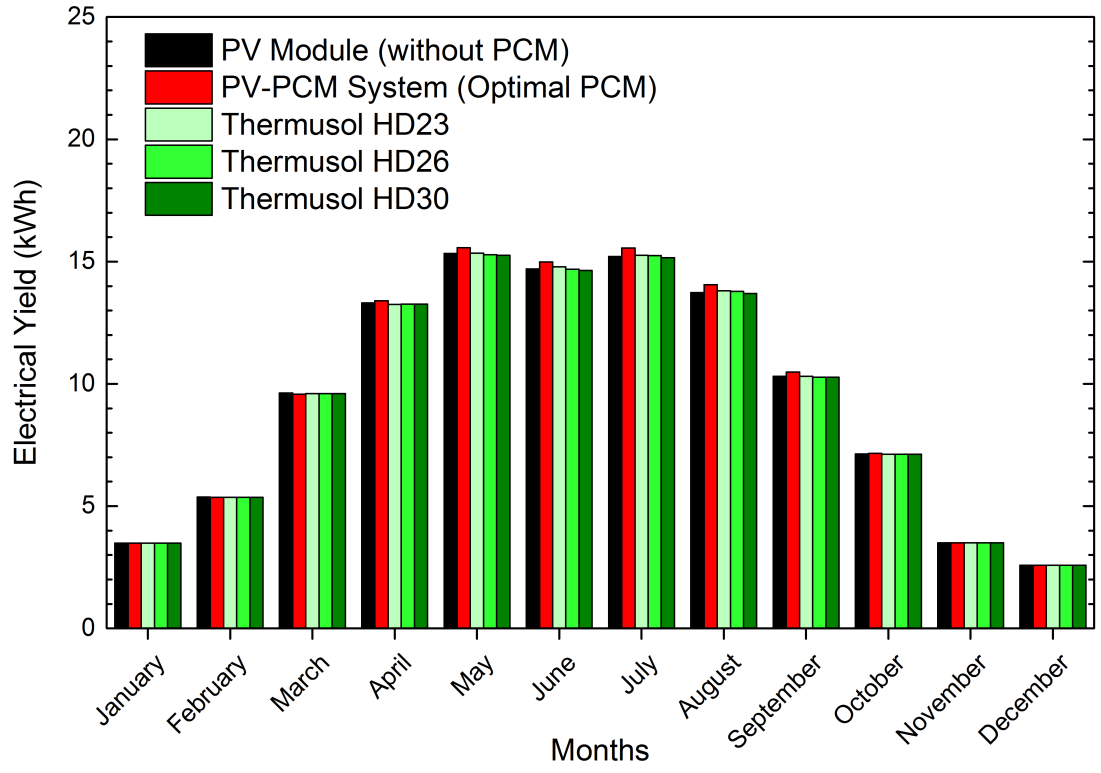

Figure 5.2: DC side electrical yield (kWh) per month for a rack-mounted PV module with 4 types of PCM configurations in Rotterdam, the Netherlands.

5.1.3. Roof-mounted module

The total DC yields per month for a roof-mounted Phaesun Sun Plus 100 S with and without the four types of PCM are displayed in figure 5.3. In this case, the lack of convective heat transfer at the back of the module or PCMs resulted in a higher temperature for the PV module and thus a lower electrical yield. However, this also means that there is a higher thermal gradient between the module and the PCM, and therefore a larger conductive heat exchange. As a consequence, the relative improvement in electrical yield is increased for the four simulated PCMs. Again, the optimized PCM is able to increase the power output of the module the most with a minimum of 0.39% in December, a maximum of 5.74% in June, and an overall improvement of 3.52%. Likewise, the change in yield is enhanced for the commercial PCMs, as can be seen in table 5.2.

5.2. Economic analysis

5.2.1. Large-scale PV-system

From the analysis regarding the performance of the PV-PCM system, it has become clear that integration of PCMs at the back of a PV module can have beneficial results in the Netherlands. However, that is only the case provided that a PCM with the right properties is chosen. In order to check whether these increases in the DC yield can be economically justified for a PV power plant, the levelized cost of electricity (LCoE) needs to determined.

The LCoE is defined as the cost per kWh of electricity produced by a power generating system, e.g. a coal plant or PV power plant. It is determined by allocating the costs of an energy plant across its full lifecycle, and can become complex depending on the number of variable costs. In a simplified case the LCoE, without taking a discount rate into account, can be defined for a PV system as:

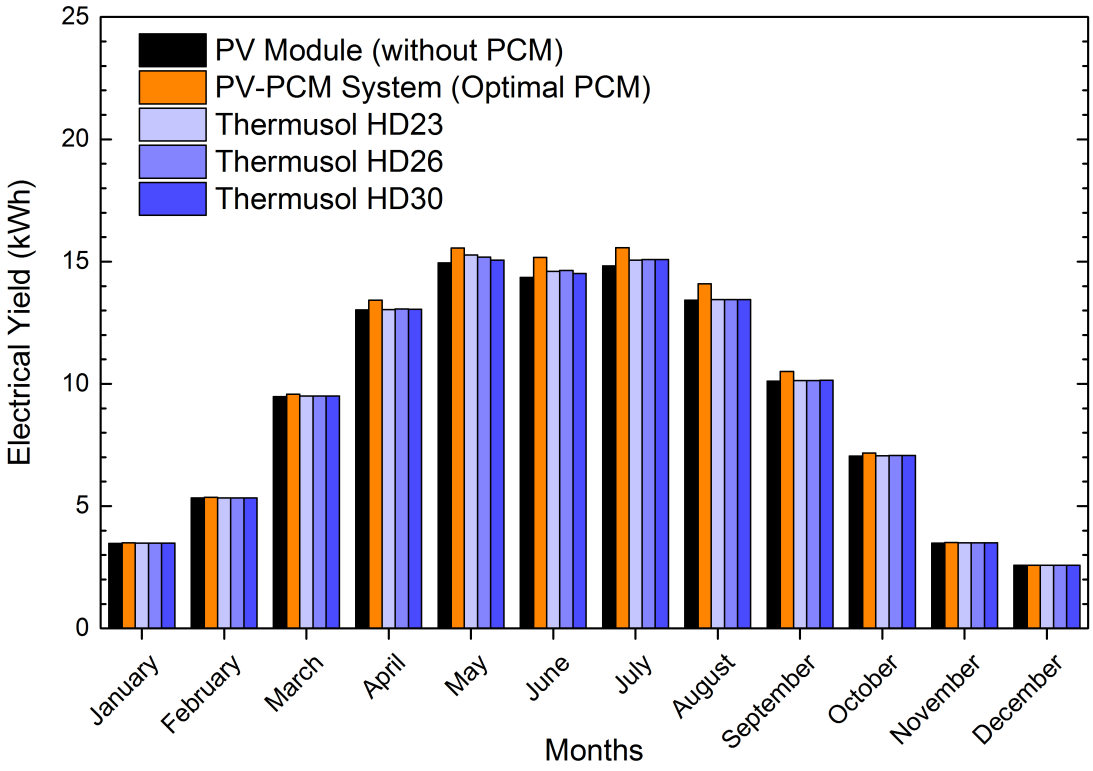

Figure 5.3: DC side electrical yield (kWh) per month for a roof-mounted PV module with 4 types of PCM configurations in Rotterdam, the Netherlands.

$$LCoE = \frac{\sum_{t=1}^{n} I_t + G_t + M_t + R_t}{\sum_{t=1}^{n} E_t} \tag{5.6}$$

The sums extend over the lifetime of the power system n, here assumed to be 25 years for the case of a PV system without PCM, and 30 years for a PV system using PCM [47]. Furthermore, I_t are the investment costs in the year t, G_t are the costs associated with connecting the system to the power grid in the year t, M_t are the operational and maintenance (O&M) costs in the year t, R_t are the costs pertaining the replacement of inverters, and E_t is the AC side electrical yield in the year t. A 2MW and 20MW PV power plant are proposed to determine the LCoE, with 440 €/kWp in module costs [52], 41.6 €/kWp for the optimized PCM, and 9.9 €/kWp for the Thermusol PCMs. The price of the PCMs was approximated to the price for the main salt component of the Thermusol PCMs, $CaCl_2$, and fitted to the size and thickness of the PV module and PCM, respectively [53].

The combination of PV modules, inverters, cables, installation costs, and optional PCM is the investment cost at t=0. Moreover, the costs for connecting the PV system to the power grid are dependant on the system size, voltage of the grid and the cable length necessary, as discussed in a cost analysis performed by research institute ECN and energy consultant DNV GL [52]. For the O&M costs, 1% of the initial investment costs per year are assumed, and 2% for the PV-PCM system. The PCM will not last as long as the PV module, with a limited thermal cycle lifetime of 1000, based on [54]. It will need to be changed approximately every 5 years, hence the extra O&M costs. Additionally, it is assumed that the inverters will need to be replaced at least once in the lifetime of the PV system. The costs of each aspect is listed in tabel 5.3.

Roof-mounted PV module									
	PV Electrical Yield [kWh]					Difference PV - PV/PCM [%]			
	No PCM	Optimal PCM	HD23	HD26	HD30	Optimal PCM	HD23	HD26	HD30
January	3.48	3.50	3.48	3.48	3.48	0.44	0.11	0.11	0.11
February	5.33	5.36	5.34	5.34	5.34	0.61	0.15	0.15	0.15
March	9.48	9.58	9.51	9.51	9.51	1.08	0.27	0.27	0.26
April	13.03	13.42	13.04	13.07	13.05	3.05	0.11	0.32	0.17
May	14.94	15.56	15.27	15.18	15.06	4.14	2.17	1.58	0.77
June	14.35	15.17	14.60	14.63	14.52	5.74	1.75	1.97	1.16
July	14.82	15.56	15.06	15.09	15.09	5.03	1.64	1.82	1.82
August	13.43	14.09	13.45	13.44	13.45	4.96	0.20	0.13	0.15
September	10.11	10.51	10.14	10.14	10.15	3.87	0.25	0.25	0.34
October	7.05	7.16	7.06	7.07	7.07	1.70	0.23	0.35	0.35
November	3.49	3.51	3.49	3.49	3.49	0.60	0.22	0.22	0.22
December	2.58	2.59	2.58	2.58	2.58	0.39	0.09	0.09	0.09
Total year	**112.08**	**116.02**	**113.03**	**113.02**	**112.78**	**3.52**	**0.85**	**0.84**	**0.62**

Table 5.2: Monthly and annual values for the DC side yield of a roof-mounted PV module and 4 types of PCM configurations, and the change in yield relative to the sole PV module. Location: Rotterdam, the Netherlands.

The annual AC side electrical yield was determined by taking the efficiencies for the inverter (95%), and MPPT (99%) into account, as well as additional losses like mismatch between modules (-1.5%), ohmic cable losses (-0.5%) and soiling (-1%) [5]. Accordingly, the yield over the total lifetime of the system was determined without consideration of a possible decrease in yield due to global warming. With the total costs and electrical yield established, the LCoE can be calculated for the PV power plant in the scenarios with and without PCM. Thermusol HD26 and HD30 have not been computed, since table 5.1 shows a decrease in yield for these PCM.

The LCoE for the optimized PCM and Thermusol HD23 is listed in table 5.4. As can be seen, the addition of a PCM to the system increases the the LCoE in both PV power plants. The extra investment in the materials and the maintenance costs do not justify the increase in electrical yield, even though the lifetime of the system was assumed to last 5 years longer. It is also clear that the additional thickness and therefore cost of the optimized PCM does not weigh up to the extra costs when compared to the thinner Thermusol HD23.

5.2.2. Residential PV system

For a consumer to consider investing in a residential PV system, the payback time is important to know. It is defined as the amount of time required to recover the cost of an investment:

$$payback\ time = \frac{initial\ investment}{annual\ return} \tag{5.7}$$

In this case, a 1kWp PV system with Phaesun Sun Plus 100 S PV modules is examined. The modules are considered to lay flush on the roof with a tilt 30^o, facing south. The cost of such a system with 10 modules, including an inverter and installation is 1.63 €/Wp [55]. Table 5.2 shows an annual DC yield of 112.08 kWh, for which the AC side yield of the 10 modules can be calculated: 1022 kWh per year. With a grid electricity price of 0.21 €/kWh [56], the average annual reduction of the electricity bill is € 215, which results in a payback time of 7 years and 7 months.

In the case of a residential system, the price of the optimized PCM and Thermusol PCMs can be approximated to be 217 €/m^2 and 50 €/m^2, respectively, amounting to 1.41 €/Wp and 0.33 €/Wp in this case. Again,

	2 MWp	**20 MWp**
Investment [€/kWp]	1023	800
PCM [€/kWp]	9.9 - 41.6	9.9 - 41.6
Grid connection [€/kWp]	205	36.2
O & M [€/kWp/y]	1-2% of investment annually	1-2% of investment annually
Inverter replacement [€/kWp]	84	84

Table 5.3: Economic parameters for the proposed large-scale PV systems in Rotterdam, the Netherlands. Prices adapted from [52].

	2 MWp	**20 MWp**
PV [€c/kWh]	6.01	4.30
PV + Optimized PCM [€c/kWh]	6.29	4.63
PCM + HD23 [€c/kWh]	6.20	4.52

Table 5.4: Levelized Cost of Electricity (LCoE) for the large-scale PV systems in Rotterdam, with and without addition of PCMs.

the payback time can be determined with the electrical yield shown in table 5.2: Optimized PCM (13.7 years), HD23/26/30 (9.1 years). Although the payback times are significantly longer for the PV-PCM systems, their lifetimes are also expected to be longer, and the electrical yield is higher as well. For the remainder of the PV system lifetimes, with and without PCM, the total amount of money saved can be determined. Assuming the previously mentioned increased lifetime of at least 5 years for the PV-PCM systems [47], the money saved with a regular PV-system, optimized PCM, HD23, HD26, and HD30 is: €3745, €3627, €4526, €4525, €4516. These monetary values, however, only include the initial investment costs and do not consider the thermal cycling lifetime of the PCMs themselves. The cost of replacement for the PCMs is expected to be dependant on whether the thermal cycling lifetime can be restored. This would mean the PCM can be reused and the overall lifetime increases and therefore price decrease.

In this chapter, the potential benefits of a PV-PCM system on the electrical yield, LCoE, and payback time have been discussed. It is evident that the benefits of electrical yield gained does not weigh up to operational/maintenance costs of the PCM. The LCoE for two large-scale PV power plants was not reduced with the addition of PCMs, and the added savings for the residential case were diminished by the O&M costs of the PCM. For future research, it is recommended to thoroughly study the effect of a PCM on the lifetime of a PV module, as well as the lifecycle of PCMs to reduce its O&M costs. Additionally, the potential application of the stored latent heat should be studied to increase the economic viability of the system.

6

Conclusions and recommendations

In this thesis, a passive cooling method has been presented to reduce the operational temperature of PV modules. The approach relies on the use of phase change materials, which can remain at a near constant temperature during their transition from solid to liquid, and vice versa. Attaching a PCM at the back of a PV module will induce a thermal gradient that can benefit the heat transfer from the module to the back. This can not only increase the electrical yield, but also benefit the total lifetime of a module.

As most of PV applications use modules based on c-Si solar cells, the focus of this work was to study the effect of PCMs on c-Si PV modules. To accomplish this, a thermal model was first developed in COMSOL Multiphysics. This software allowed for comprehensive simulations of a PV module with and without addition of PCMs by computing of all heat transfer mechanisms and phase change physics involved. After benchmarking of the models with field measurements from literature, simulations could be run for various weather conditions. In order to increase the accuracy of the model, field measurements should be performed whereby more parameters influencing the module temperature are known.

Application of the model revealed that PCMs can also increase the peak PV temperature if the PCM properties are not favourable for the corresponding climate. Based on this, a optimization study was performed for an average winter and summer day in Rotterdam, the Netherlands. Optimized PCM properties were found that could reduce the peak operational temperature by 4.5^{o}C on an average day in summer. The described method can help find an appropriate PCM for different climatic conditions. To reduce the amount of time it takes to optimize the properties, it is recommended to automate the parametric sweeps for these time-dependent studies in COMSOL Multiphysics.

An experimental set-up was built to measure the operational temperature of a PV module with commercially available PCMs under a Large Area Solar Simulator (LASS). These were able to reduce the average module temperature by 30-36°C. Performance of the system can be improved by increasing the area coverage of the PCM at the back of the module. This will also increase the timeframe for the measurements. Without full coverage in this study, hotspots were created causing a non-uniform temperature distribution across the surface.

An examination of the effect of various PCMs on the electrical yield of a PV module in Rotterdam showed that the annual change in yield for a rack-mounted module can fluctuate between -0.31% and 1.23%, depending on the type of PCM used. For a roof-mounted PV module using the same types of PCM, the annual yield change improves as the reference case without PCM operates at a higher temperature: 0.62%- 3.52%. The ensuing economic analysis demonstrated that the gains in electrical yield and module lifetime are not enough to justify the use of PCMs. The costs of the PCMs that have to be replaced or maintained every five years outweigh the potential benefits. For future research, it is recommended to extensively study the effect of a lower operational PV temperature on its lifetime. Additionally, the utilization of the stored latent heat should be considered to increase the economic viability of the system.

A

PV module datasheet

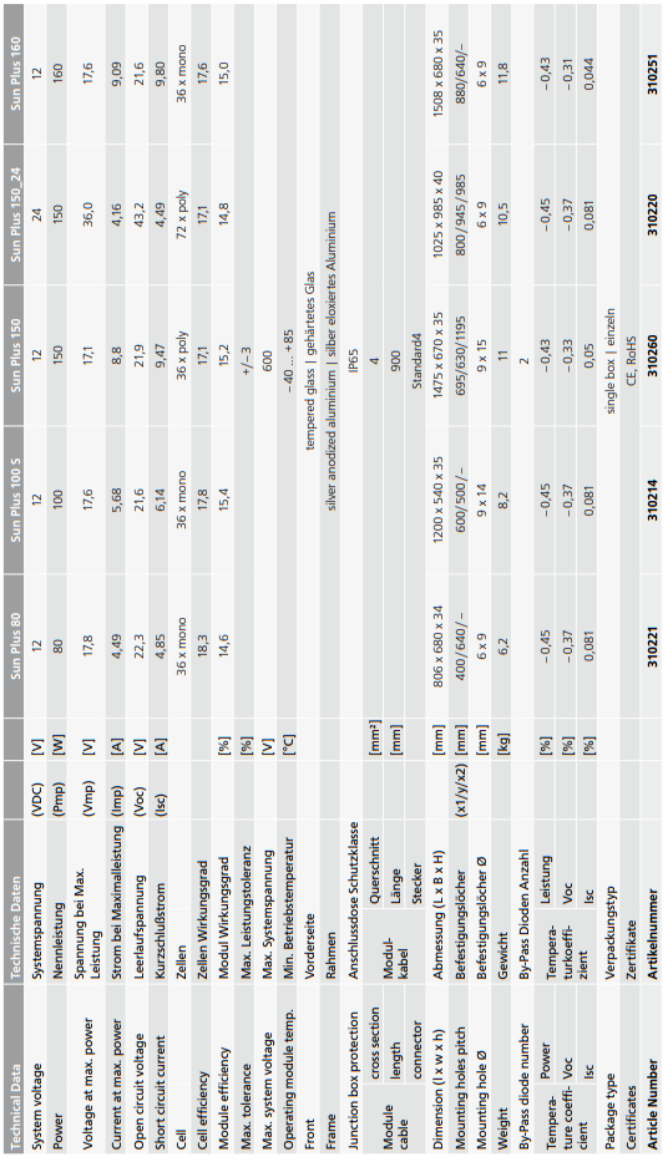

Technical Data				Sun Plus 80	Sun Plus 100 S	Sun Plus 150	Sun Plus 150_24	Sun Plus 160
System voltage	Systemspannung	(VDC)	[V]	12	12	12	24	12
Power	Nennleistung	(Pmp)	[W]	80	100	150	150	160
Voltage at max. power	Spannung bei Max. Leistung	(Vmp)	[V]	17,8	17,6	17,1	36,0	17,6
Current at max. power	Strom bei Maximalleistung	(Imp)	[A]	4,49	5,68	8,8	4,16	9,09
Open circuit voltage	Leerlaufspannung	(Voc)	[V]	22,3	21,6	21,9	43,2	21,6
Short circuit current	Kurzschlußstrom	(Isc)	[A]	4,85	6,14	9,47	4,49	9,80
Cell	Zellen			36 x mono	36 x mono	36 x poly	72 x poly	36 x mono
Cell efficiency	Zellen Wirkungsgrad		[%]	18,3	17,8	17,1	17,1	17,6
Module efficiency	Modul Wirkungsgrad		[%]	14,6	15,4	15,2	14,8	15,0
Max. tolerance	Max. Leistungstoleranz		[%]			+/–3		
Max. system voltage	Max. Systemspannung		[V]			600		
Operating module temp.	Min. Betriebstemperatur		[°C]			–40 ... +85		
Front	Vorderseite					tempered glass | gehärtetes Glas		
Frame	Rahmen					silver anodized aluminium | silber eloxiertes Aluminium		
Junction box protection	Anschlussdose Schutzklasse					IP65		
Module cable	cross section	Querschnitt	[mm²]			4		
	length	Länge	[mm]			900		
	connector	Stecker				Standard4		
Dimension (l x w x h)	Abmessung (L x B x H)		[mm]	806 x 680 x 34	1200 x 540 x 35	1475 x 670 x 35	1025 x 985 x 40	1508 x 680 x 35
Mounting holes pitch	Befestigungslöcher	(x1/y/x2)	[mm]	400/640/–	600/500/–	695/630/1195	800/945/985	880/640/–
Mounting hole Ø	Befestigungslöcher Ø		[mm]	6 x 9	9 x 14	9 x 15	6 x 9	6 x 9
Weight	Gewicht		[kg]	6,2	8,2	11	10,5	11,8
By-Pass diode number	By-Pass Dioden Anzahl					2		
Tempera-ture coeffi-cient	Power	Leistung	[%]	–0,45	–0,45	–0,43	–0,45	–0,43
	Voc		[%]	–0,37	–0,37	–0,33	–0,37	–0,31
	Isc		[%]	0,081	0,081	0,05	0,081	0,044
Package type	Verpackungstyp					single box | einzeln		
Certificates	Zertifikate					CE, RoHS		
Article Number	**Artikelnummer**			**310221**	**310214**	**310260**	**310220**	**310251**

Figure A.1: Datasheet for the Phaesun Sun Plus 100 S monocrystalline PV module used in this thesis.

B

Spectral irradiance of the LASS

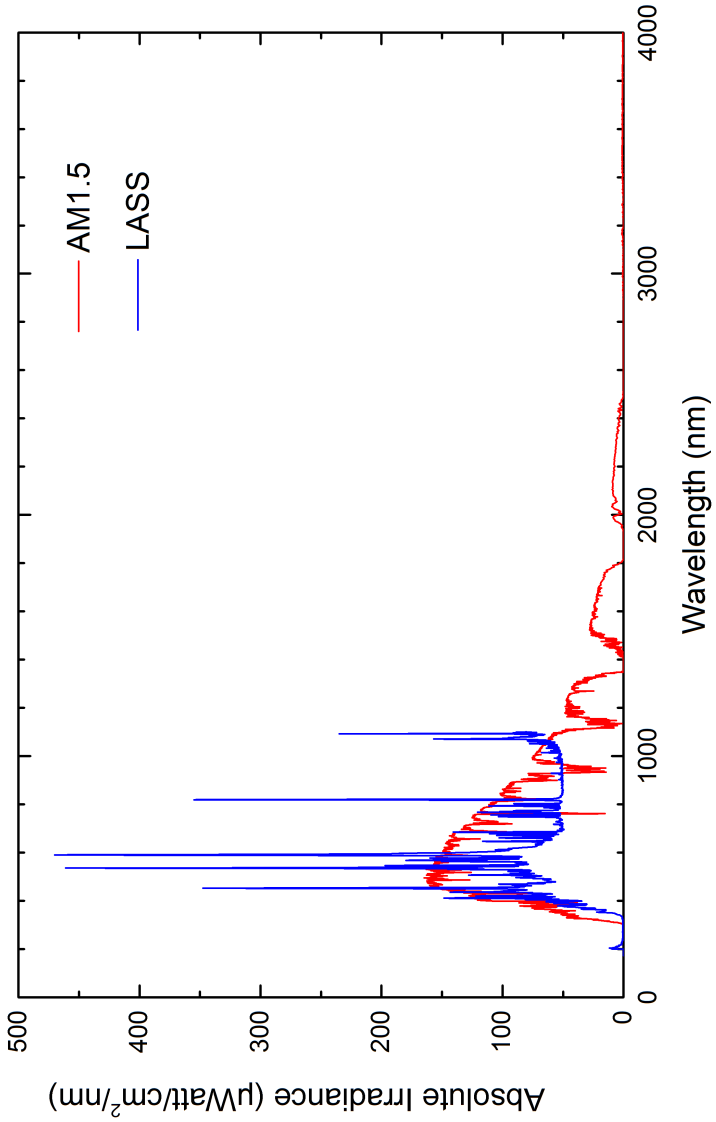

Figure B.1: Comparison of the AM1.5 spectrum and the available data for the Large Area Solar Simulator.

Bibliography

[1] Key world energy statistics 2018. Technical report, International Energy Agency, 2018.

[2] Bp energy outlook 2035. Technical report, BP p.l.c., 2015.

[3] Intergovernmental Panel on Climate Change. *Climate Change 2013 – The Physical Science Basis: Working Group I Contribution to the Fifth Assessment Report of the Intergovernmental Panel on Climate Change*. Cambridge University Press, 2014.

[4] Photovoltaic report. Technical report, Fraunhofer Institute for Solar Energy Systems (ISE), 2017.

[5] Arno Smets, Klaus Jäger, Olindo Isabella, R.A.C.M.M. Van Swaaij, and Miro Zeman. *Solar Energy - The physics and engineering of photovoltaic conversion, technologies and systems*. UIT Cambridge, 02 2016.

[6] A. Hasan, S.J. McCormack, M.J. Huang, and B. Norton. Evaluation of phase change materials for thermal regulation enhancement of building integrated photovoltaics. *Solar Energy*, 84(9):1601 – 1612, 2010.

[7] Emeka H. Amalu, David J. Hughes, F. Nabhani, and Julie Winter. Thermo-mechanical deformation degradation of crystalline silicon photovoltaic (c-si pv) module in operation. *Engineering Failure Analysis*, 84:229 – 246, 2018.

[8] Musa T. Zarmai, N.N. Ekere, C.F. Oduoza, and Emeka H. Amalu. A review of interconnection technologies for improved crystalline silicon solar cell photovoltaic module assembly. *Applied Energy*, 154:173 – 182, 2015.

[9] John H. Wohlgemuth. Reliability of pv systems. *Proceedings of SPIE2*, 7048:704802–2, 2008.

[10] DuPont. What makes up a solar panel. [Online; accessed 8-March-2018].

[11] E Radziemska. The effect of temperature on the power drop in crystalline silicon solar cells. *Renewable Energy*, 28(1):1–12, 2003.

[12] Akira Usami, Shiro Seki, Yuichi Mita, Hiromu Kobayashi, Hajime Miyashiro, and Nobuyuki Terada. Temperature dependence of open-circuit voltage in dye-sensitized solar cells. *Solar Energy Materials and Solar Cells*, 93(6):840 – 842, 2009. 17th International Photovoltaic Science and Engineering Conference.

[13] Open Photovoltaics Analysis Platform. I-v characteristics. [Online; accessed 11-January-2018].

[14] K. Araki, H. Uozumi, and M. Yamaguchi. A simple passive cooling structure and its heat analysis for 500 times; concentrator pv module. In *Conference Record of the Twenty-Ninth IEEE Photovoltaic Specialists Conference, 2002.*, pages 1568–1571, May 2002.

[15] J.K. Tonui and Y. Tripanagnostopoulos. Performance improvement of pv/t solar collectors with natural air flow operation. *Solar Energy*, 82(1):1 – 12, 2008.

[16] Y. Tripanagnostopoulos, Th. Nousia, M. Souliotis, and P. Yianoulis. Hybrid photovoltaic/thermal solar systems. *Solar Energy*, 72(3):217 – 234, 2002.

[17] Liping Liu, Li Zhu, Yiping Wang, Qunwu Huang, Yong Sun, and Zhaojiang Yin. Heat dissipation performance of silicon solar cells by direct dielectric liquid immersion under intensified illuminations. *Solar Energy*, 85:922–930, 2011.

[18] C.R. Russell. Optical concentrator and cooling system for photovoltaic cells, October 4 1977. US Patent 4,052,228.

[19] Haijun Xiang, Yiping Wang, Li Zhu, Xinyue Han, Yong Sun, and Zhengjian Zhao. 3d numerical simulation on heat transfer performance of a cylindrical liquid immersion solar receiver. *Energy Conversion and Management*, 64:97 – 105, 2012. IREC 2011, The International Renewable Energy Congress.

[20] G.F. Russell. Uniform surface temperature heat pipe and method of using the same, March 16 1982. US Patent 4,320,246.

[21] HUANG M. J., EAMES P. C., and NORTON B. Phase change materials for limiting temperature rise in building integrated photovoltaics. *Solar energy*, 80(9):1121–1130, 2006.

[22] Dengfeng Du, Jo Darkwa, and Georgios Kokogiannakis. Thermal management systems for photovoltaics (pv) installations: A critical review. *Solar Energy*, 97:238 – 254, 2013.

[23] M.C. Browne, B. Norton, and S.J. McCormack. Phase change materials for photovoltaic thermal management. *Renewable and Sustainable Energy Reviews*, 47:762 – 782, 2015.

[24] Chand Jotshi, D Goswami, and J J. Tomlinson. Solar thermal energy storage in phase change material. *Solar Energy*, pages 13–18, 01 1992.

[25] Ming Jun Huang. *The application of computational fluid dynamics (CFD) to predict the thermal performance of phase change materials for the control of photovoltaic cell temperature in buildings*. PhD thesis, Faculty of Engineering and Built Environment University of Ulster, 2002.

[26] A. Hasan, S.J. McCormack, M.J. Huang, and B. Norton. Characterization of phase change materials for thermal control of photovoltaics using differential scanning calorimetry and temperature history method. *Energy Conversion and Management*, 81:322 – 329, 2014.

[27] Ahmet Sarı, Alper Bicer, Amir Al-Ahmed, Fahad A. Al-Sulaiman, Md. Hasan Zahir, and Shamseldin A. Mohamed. Silica fume/capric acid-palmitic acid composite phase change material doped with cnts for thermal energy storage. *Solar Energy Materials and Solar Cells*, 179:353 – 361, 2018.

[28] Ahmet Sarı and Ali Karaipekli. Preparation and thermal properties of capric acid/palmitic acid eutectic mixture as a phase change energy storage material. *Materials Letters*, 62(6):903 – 906, 2008.

[29] Ali Karaipekli and Ahmet Sari. Capric acid and palmitic acid eutectic mixture applied in building wallboard for latent heat thermal ener gy storage. *Journal of scientific and industrial research*, 11 2014.

[30] Harald Mehling and Luisa F. Cabeza. *Heat and Cold Storage with PCM: An Up to Date Introduction Into Basics and Applications*. Springer, 01 2008.

[31] M.J. Huang, P.C. Eames, and B. Norton. Thermal regulation of building-integrated photovoltaics using phase change materials. *International Journal of Heat and Mass Transfer*, 47(12):2715 – 2733, 2004.

[32] Ahmed Hassan, S.J. McCormack, M.J. Huang, and Brian Norton. Energy and cost saving of a photovoltaic-phase change materials (pv-pcm) system through temperature regulation and performance enhancement of photovoltaics. *Energies*, 7:1318–1331, 03 2014.

[33] Yuli Setyo Indartono, Aryadi Suwono, and Fendy Yuseva Pratama. Improving photovoltaics performance by using yellow petroleum jelly as phase change material. *International Journal of Low-Carbon Technologies*, 11, 12 2014.

[34] Yuli Setyo Indartono, S D Prakoso, Aryadi Suwono, Ilman Zaini, and B Fernaldi. Simulation and experimental study on effect of phase change material thickness to reduce temperature of photovoltaic panel. *IOP Conference Series: Materials Science and Engineering*, 88:012049, 09 2015.

[35] T.K. Bergman and Frank P. Incropera. *Fundamentals of heat and mass transfer*. Wiley, 2011.

[36] J.A. Palyvos. A survey of wind convection coefficient correlations for building envelope energy systems' modeling. *Applied Thermal Engineering*, 28(8):801 – 808, 2008.

[37] Müslüm Arıcı, Feyza Bilgin, Sandro Nižetić, and Agis M. Papadopoulos. Phase change material based cooling of photovoltaic panel: A simplified numerical model for the optimization of the phase change material layer and general economic evaluation. *Journal of Cleaner Production*, 189:738 – 745, 2018.

[38] John Crepeau. Josef stefan and his contributions to heat transfer. *2008 Proceedings of the ASME Summer Heat Transfer Conference, HT 2008*, 3, 01 2008.

[39] R. Santbergen, T. Meguro, T. Suezaki, G. Koizumi, K. Yamamoto, and M. Zeman. Genpro4 optical model for solar cell simulation and its application to multijunction solar cells. *IEEE Journal of Photovoltaics*, 7(3):919–926, May 2017.

[40] Malte Ruben Vogt. *Development of Physical Models for the Simulation of Optical Properties of Solar Cell Modules*. PhD thesis, Fakultät für Mathematik und Physik der Gottfried Wilhelm Leibniz Universität Hannover, 2015.

[41] R. Santbergen and R.J.C. van Zolingen. The absorption factor of crystalline silicon pv cells: A numerical and experimental study. *Solar Energy Materials and Solar Cells*, 92(4):432 – 444, 2008.

[42] Valerio Lo Brano, Giuseppina Ciulla, Antonio Piacentino, and Fabio Cardona. Finite difference thermal model of a latent heat storage system coupled with a photovoltaic device: Description and experimental validation. *Renewable Energy*, 68:181 – 193, 2014.

[43] N. Peter, O.E. Kabu, K. Stephen, and D. Anthony. 3d finite element method modeling and simulation of the temperature of crystalline photovoltaic module. *International Journal of Research in Engineering and Technology*, 04(9):378 – 384, 2015.

[44] Walter Frei. Thermal modeling of phase-change materials with hysteresis. [Online; accessed 18-October-2018].

[45] M. Zaaijer. Introduction to wind energy - wind climate and energy production (presentation).

[46] Florian Kleiner, Konrad Posern, and Andrea Osburg. Thermal conductivity of selected salt hydrates for thermochemical solar heat storage applications measured by the light flash method. *Applied Thermal Engineering*, 113:1189 – 1193, 2017.

[47] Patricia Royo, Víctor J. Ferreira, Ana M. López-Sabirón, and Germán Ferreira. Hybrid diagnosis to characterise the energy and environmental enhancement of photovoltaic modules using smart materials. *Energy*, 101:174 – 189, 2016.

[48] OC Autarkis. https://www.orangeclimate.com/nl/ocautarkis. [Online; accessed 12-January-2019].

[49] Eternal Sun. Large area solar simulator. [Online; accessed 24-October-2018].

[50] KAN Ltd. http://kan.bg/wp-content/uploads/2013/03/solar-geothermal-power-plant-nevada-1024x577.jpg. [Online; accessed 10-January-2019].

[51] Romag. https://www.romag.co.uk/solar/roof-integrated-pv/. [Online; accessed 10-January-2019].

[52] Luuk Beurskens and Jasper Lemmers. Kostenonderzoek zonne-energie sde+ 2018 (zon-pv vanaf 15 kwp en zonthermie vanaf 140 kw). [Online; accessed 12-January-2019].

[53] Alibaba CaCl2. [Online; accessed 12-January-2019].

[54] V.V. Tyagi and D. Buddhi. Thermal cycle testing of calcium chloride hexahydrate as a possible pcm for latent heat storage. *Solar Energy Materials and Solar Cells*, 92(8):891 – 899, 2008.

[55] Milieu Centraal. Kosten en opbrengst zonnepanelen. [Online; accessed 12-January-2019].

[56] Pricewise. kwh-prijs. [Online; accessed 12-January-2019].